Summer 2013

Detecting and locating electronic devices using their unintended electromagnetic emissions

Colin Stagner

Department: Electrical and Computer Engineering

DETECTING AND LOCATING ELECTRONIC DEVICES USING THEIR UNINTENDED ELECTROMAGNETIC EMISSIONS

by

COLIN BLAKE STAGNER

A DISSERTATION

Presented to the Faculty of the Graduate School of the

MISSOURI UNIVERSITY OF SCIENCE AND TECHNOLOGY

In Partial Fulfillment of the Requirements for the Degree

DOCTOR OF PHILOSOPHY

in

ELECTRICAL & COMPUTER ENGINEERING

2013

Approved by

Dr. Steve Grant, Advisor
Dr. Daryl Beetner
Dr. Kurt Kosbar
Dr. Reza Zoughi
Dr. Bruce McMillin

ABSTRACT

Electronically-initiated explosives can have unintended electromagnetic emissions which propagate through walls and sealed containers. These emissions, if properly characterized, enable the prompt and accurate detection of explosive threats. The following dissertation develops and evaluates techniques for detecting and locating common electronic initiators. The unintended emissions of radio receivers and microcontrollers are analyzed. These emissions are low-power radio signals that result from the device's normal operation.

In the first section, it is demonstrated that arbitrary signals can be injected into a radio receiver's unintended emissions using a relatively weak stimulation signal. This effect is called stimulated emissions. The performance of stimulated emissions is compared to passive detection techniques. The novel technique offers a 5 to 10 dB sensitivity improvement over passive methods for detecting radio receivers.

The second section develops a radar-like technique for accurately locating radio receivers. The radar utilizes the stimulated emissions technique with wideband signals. A radar-like system is designed and implemented in hardware. Its accuracy tested in a noisy, multipath-rich, indoor environment. The proposed radar can locate superheterodyne radio receivers with a root mean square position error less than 5 meters when the SNR is 15 dB or above.

In the third section, an analytic model is developed for the unintended emissions of microcontrollers. It is demonstrated that these emissions consist of a periodic train of impulses. Measurements of an 8051 microcontroller validate this model. The model is used to evaluate the noise performance of several existing algorithms. Results indicate that the pitch estimation techniques have a 4 dB sensitivity improvement over epoch folding algorithms.

ACKNOWLEDGMENTS

The author would like to thank his advisor, Dr. Steve Grant, for his insightful guidance throughout each stage of these projects. Dr. Grant, who introduced me to the realm of signal processing, assisted greatly with many of the measurements found in this text. His endless patience, and willingness to share his decades of research experience, are most appreciated. I would also like to thank Dr. Daryl Beetner's minute attention to detail and continuous revisions, which have greatly improved the quality of my writing and sped my papers along to publication.

My friends and fellow PhDs, Dr. Chris Osterwise and Dr. Dan Krus, have been with me every step of the way, and their keen observations have kept my dissertation on track. Cisa, who is wise beyond her years, has offered me counsel and guidance which has improved every aspect of my life. Our dog Lea should also be recognized for her brief—though futile—attempt at grading.

Considerable financial support for this research was provided by the U.S. Department of Homeland Security under Award Number 2008-ST-061-ED0001, the National Science Foundation under Grant No. 0855878, and the Wilkens Missouri Endowment. The author would also like to thank the years of steady financial support provided by Missouri S&T's Chancellor's Fellowship program, which has enabled me to complete my required coursework.

Credit is also due to the volunteer developers of GNU Radio, GNU Octave, and the various other open source projects which are an integral part of this research. Their time and efforts have enabled this contribution to science.

Finally, I would like to thank DeeDee for her unwavering dedication and boundless capacity for self-expression: you make each day an adventure unto itself.

TABLE OF CONTENTS

Page

LIST OF ILLUSTRATIONS

LIST OF TABLES

1. INTRODUCTION

Remote detection of improvised explosive devices is essential to guaranteeing safety in conflict-prone environments. At present, there are three main techniques for detecting explosive devices: manual search, portal screening, and chemical trace detection. Manual search techniques utilize explosives ordinance disposal (EOD) technicians to find and neutralize explosives. Clearing an area is a time-consuming, dangerous task which can expose personnel and resources, such as robots, to risk. In portal screening techniques, a secure area is defined, and persons entering the area are subject to a thorough search. This technique results in large delays and great expense: the United States spends $4.8 billion U.S. dollars per year on security checkpoints for its airports [2].

Both of these search methods are often augmented with some type of explosives-detection sensor. Chemical traces are the most specific indication that explosives are present, and others have developed a number of different techniques for detecting them. By characterizing the chemical composition and behavior of high-explosives, such as ammonium nitrate [3], it is possible to build more reliable sensors. Terahertz imaging techniques offer improved portal screening with an inherent explosives-detection capability [4].

Sensors that are capable of detecting explosives from outside of their effective range are an important, emerging area of research. This search strategy is commonly referred to as *standoff detection*. These sensors must cope with the low signal-to-noise ratio (SNR) which is inherent to long-range detection. Raman spectroscopy is one such technique. It has the potential to detect chemical traces on surfaces, using lasers, at great distances [5].

These techniques have inherent disadvantages, however. Scanning a large area can be extremely time consuming. Obstacles like hills, trees, and buildings can prevent detection. All chemical trace systems, including canines, have difficulty detecting explosives which are housed in air-tight containers [6]. Indirect methods, which detect the non-explosive components, can be useful in these situations.

Explosive devices typically contain at least three components: propellant, a payload, and an initiator. Each of these components, which are shown conceptually in Figure 1.1, provides a different opportunity for detection. Chemical traces are the most specific indication that explosives are present, but the payload and initiator can have specific, detectable environmental signatures as well.

One way to indirectly detect potential explosive devices is to detect the initiator. Explosive devices are commonly initiated using proximity sensors or remote triggers [7, 8]. These initiators are electronic devices which generate and process high-frequency signals. Such signals can radiate from resonant features in the device's printed circuit board (PCB) and packaging, escaping into the environment as *unintended electromagnetic emissions*.

Unlike chemical traces, electromagnetic emissions can propagate freely through closed containers and vehicles. Others have demonstrated that these emissions can

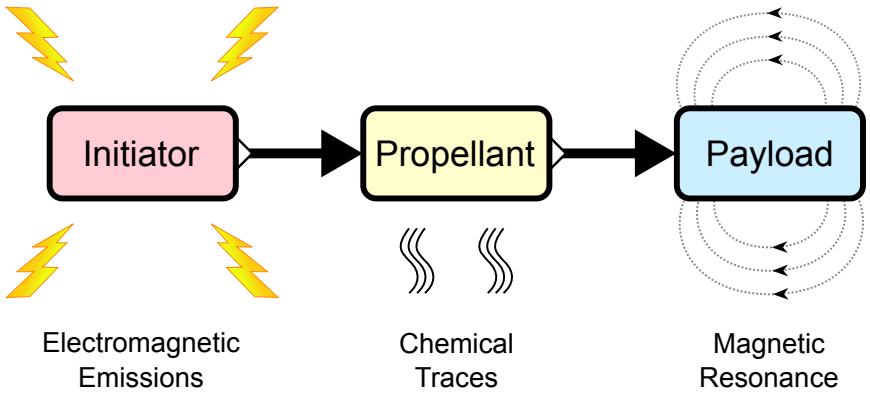

Figure 1.1: Each component of an explosive device has a specific environmental signature.

reveal information about a device's purpose and internal state [9], making it possible to determine what types of devices are present. By detecting potential initiators, it is possible to infer the presence of an explosive threat. This approach makes non-line-of-sight device detection feasible at relatively long range.

In order to provide a substantial advantage over the direct methods, an electronic initiator detector must offer high sensitivity and selectivity. A high-sensitivity detector should be capable of detecting weak, unintended electromagnetic emissions—the power of which is strictly limited by regulation [10]. While an extraordinary variety of electronic devices exist, a detector should be capable of separating devices which pose an explosive-related threat from devices which do not. Selectivity and sensitivity can be improved by using specific knowledge of the emissions' characteristics.

The purpose of this work is to improve techniques for detecting specific types of electronic initiators. Radio receivers of every variety, such as doorbells, automobile keyfobs, two-way radios, and cellular telephones, can be used as remote initiators [8,11]. Devices may also incorporate microcontrollers and other clocked, digital logic systems for either timing or control purposes. This dissertation includes three papers on the detection, location, and identification of these electronic devices.

The first paper, which was originally published as [12], presents a new technique for detecting superheterodyne radio receivers. This technique, which is known as stimulated emissions, was originally developed for super-regenerative receivers. The extension allows stimulated emissions to work with a wide variety of new devices. Numerical simulations indicate that the theoretical performance of stimulated emissions far exceeds that of existing, passive techniques.

In the second paper, new measurements suggest that superheterodyne receivers are sensitive to a much wider band of frequencies than they are designed to

receive. As published in [13], this new information enables the development of a time-of-arrival technique for locating radio receivers. Radar theory is combined with the stimulated emissions technique to determine the range to radio receivers. A hardware test platform is developed, and the accuracy of this technique is tested in both indoor and outdoor environments.

For the third paper, techniques are tested for positively identifying microcontrollers using their unintended electromagnetic emissions. It is demonstrated that microcontrollers have clock-dependent emissions that are impulsive and periodic. An autoregressive model is developed for simulating, and for detecting, clock emissions. Several algorithms, including one novel algorithm, are proposed for detecting these emissions. The applicability and usefulness of each algorithm as a clock-circuit detector is considered and tested in a simulated environment.

2. DETECTING SUPERHETERODYNE RECEIVERS

Advances in electronics and RF design have made radio receivers smaller, cheaper, and more common than ever before. These new devices enable a plethora of innovative applications, but they can also be used maliciously to initiate explosives. One way to indirectly locate potential explosive devices is to locate the radio receiver, thus mitigating this threat. Radio receivers use many different high frequency signals that readily escape into the environment, resulting in unintended electromagnetic emissions. It is possible to detect radio receivers using these unintended electromagnetic emissions [14–17].

While modern devices use a variety of radio receiver designs, the superheterodyne receiver remains one of the most common. Superheterodyne receivers translate high-frequency signals to a lower frequency, making them ideal for reproducing high-quality voice and data signals. Broadcast radio receivers, cellular phones, and two-way radios frequently incorporate superheterodyne receivers.

It is well-known that superheterodyne receivers have strong, sinusoidal local oscillator (LO) emissions. Others have demonstrated that these emissions can be detected using periodograms [15]. In this approach, a signal which potentially contains unintended emissions is sampled, and its periodogram is computed. Each bin is compared with a threshold, and the detector is satisfied if this threshold is exceeded. Existing research focuses on broadcast radio receivers, such as the television sets studied in [15].

Unlike television sets, two-way radios and other battery-powered devices are intended for intermittent use. As shown herein, two-way radios cycle their local oscillators on and off to conserve power. This cycling makes the emissions non-stationary, greatly decreasing the effectiveness of periodogram techniques. The periodogram

technique is also likely to be susceptible to interfering signals, since only the level of emissions, in a narrow band, is observed. Improved detection methods are needed.

Unintended emissions can reveal information about an electronic device's internal state [9], and radio receivers are no exception. Unlike other types of devices, however, radio receivers are highly responsive to weak stimulation signals. Transmitting a known stimulation signal to a receiver can change its unintended emissions in a predictable manner. It is possible to detect radio receivers by comparing their unintended emissions with the stimulation signal. This technique is called *stimulated emissions* detection. This approach is similar to harmonic detection techniques, which illuminate the electronic device with a strong stimulation and look for "reflected" harmonics caused by interaction with non-linear electronic components. Since the proposed technique modifies the intended signals within the device, it can use a much lower power stimulation, can work at a longer range, and will have fewer false-alarms than harmonic detection.

Others have developed stimulated emissions detectors for super-regenerative receivers [14]. These systems offer improved sensitivity over unstimulated, passive detectors, but they are incapable of detecting superheterodyne receivers. Existing detectors affect the quenching signal in a super-regenerative circuit [17], which is not present in superheterodyne receivers. Since stimulated emissions detectors outperform passive detectors for super-regenerative receivers, it is worthwhile to develop stimulated emissions techniques for superheterodyne receivers.

The following paper describes the development of a superheterodyne radio detector. Real radio receivers were measured during operation, and it is demonstrated that certain unintended emissions have an identical complex envelope to the stimulation signal. A stimulated emissions detector, which is detailed in Section 2.2.2, was developed using matched filters. The performance of the stimulated emissions detector was compared with existing methods [15] using artificially-generated emissions.

The stimulated emissions approach offers substantial quantitative and qualitative advantages over existing methods, increasing the energy of the emissions and eliminating false-positives caused by non-radio devices.

2.1. MEASURING THE UNINTENDED EMISSIONS

Superheterodyne radios use mixers to perform channel selection and frequency translation in a single step. Consider a bandpass radio signal $x(t)$ centered at f_{RF} Hz. Multiplying this signal with a cosine at f_{LO} Hz results in an output of $y(t)$ such that

$$y(t) = x(t)\cos\left(2\pi f_{LO}t\right) \tag{2.1}$$

By the modulation theorem [18], the frequency domain output $Y(f) = \mathscr{F}\left\{y(t)\right\}$ is:

$$Y(f) = \frac{1}{2}\left(X(f - f_{LO}) + X(f + f_{LO})\right) \tag{2.2}$$

Thus, the mixer produces two frequency-shifted copies of the signal, centered at f_{IF} and f_H, such that

$$f_{IF} = f_{RF} - f_{LO} \tag{2.3}$$

$$f_H = f_{RF} + f_{LO} \tag{2.4}$$

Superheterodyne receivers translate radio signals to a fixed intermediate frequency, f_{IF}, by choosing the local oscillator frequency, f_{LO}, according to (2.3).

The mixer, shown in Figure 2.1, creates several different signals of interest. In order to make f_{IF} relatively low, superheterodyne receivers must generate a high frequency f_{LO}. In addition to down-mixing the radio signal to f_{IF}, the mixer also up-mixes the signal to f_H. This high frequency output is an unwanted byproduct,

but it is easily removed with a low-order filter. Superheterodyne receivers frequently use two or more mixer stages, and the operating frequencies of the second stage are known herein as f_{IF_2} and f_{LO_2}.

Any of these frequencies, including f_{LO}, f_{IF}, f_{LO_2}, f_{H_2}, and f_H, can escape from the radio receiver as unintended emissions, as will be demonstrated in the following paragraphs.

2.1.1. Near-Field Analysis. Studies of the emissions from superheterodyne receivers were performed using General Mobile Radio Service (GMRS) transceivers. GMRS radios are popular, "walkie-talkie" style radios with a range of roughly five miles [19]. Their low cost, long battery life, built-in squelch codes, and long range make them ideal for a number of uses, but they are also small and easily concealed about a person or device. GMRS radios often incorporate superheterodyne

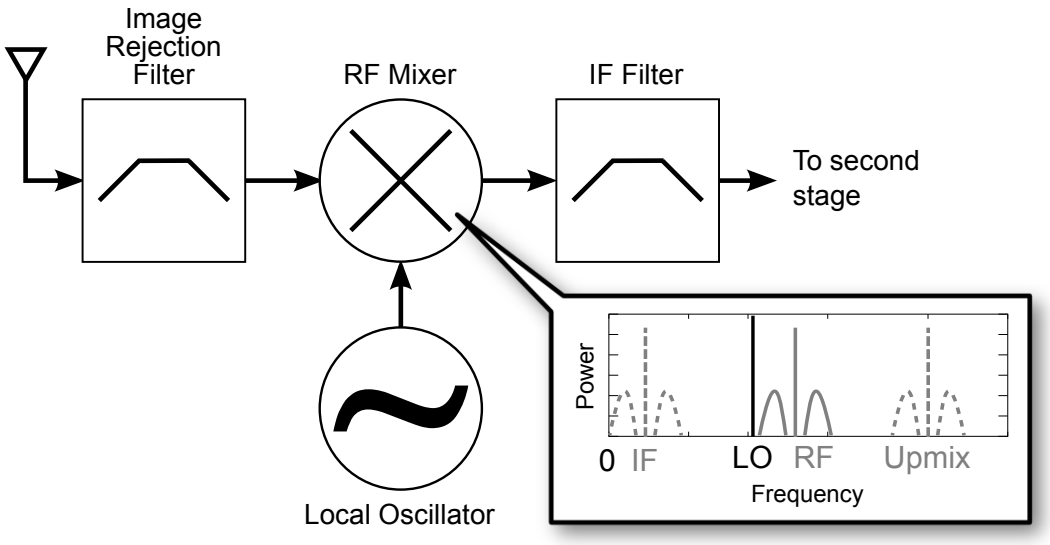

Figure 2.1: A superheterodyne receiver front-end. In a superheterodyne receiver, the mixer shifts the RF input both down in frequency (IF component) and up in frequency (up-mixing component). These signals are plotted conceptually above. The receiver itself keeps only the IF component; the other signals are filtered out. The up-mixing component has a high frequency, and—before it can be filtered out—tends to radiate into the environment.

receivers that have strong stimulated emissions, making them an ideal candidate for stimulated emissions research.

Several GMRS radios were tested in the near-field to characterize their unintended emissions frequencies. The radios were placed in a transverse electromagnetic (TEM) cell, and their unintended emissions were measured with a spectrum analyzer. To determine the difference between unstimulated and stimulated emissions, each radio was tuned to an unoccupied channel and tested with both no stimulation and with a continuous wave (CW) stimulation. Frequency domain emissions from one such test are shown in Figure 2.2. By comparing measurements with and without a stimulation, it is possible to determine if a signal is a local oscillator or a mixer output.

Local oscillator signals are always present, regardless of whether or not the radio is receiving a signal. Superheterodyne receivers generate LO signals using purely internal clock sources, such as crystal oscillators [20]. Since these oscillators are designed to maintain a constant frequency—even in the presence of strong radio signals—it is unlikely that a typical radio signal will affect LO emissions. Since it is difficult to determine if a radio signal is present without down-mixing, superheterodyne receivers must keep their LOs active—even when no radio signal is present. Any local oscillator emissions will therefore be frequency-invariant and will not require a stimulation signal.

Unlike local oscillator signals, mixer outputs depend significantly on stimulation input signals. From (2.2), it is clear that the mixer outputs an attenuated copy of the input signal. If the radio is unstimulated, $x(t) \to 0$ and the mixer's output $y(t) \to 0$, regardless of the local oscillator signal's behavior. If the radio is stimulated, then the mixer outputs should contain a frequency-shifted copy of the stimulation signal—an effect that is tested in the following section. Mixer output emissions are

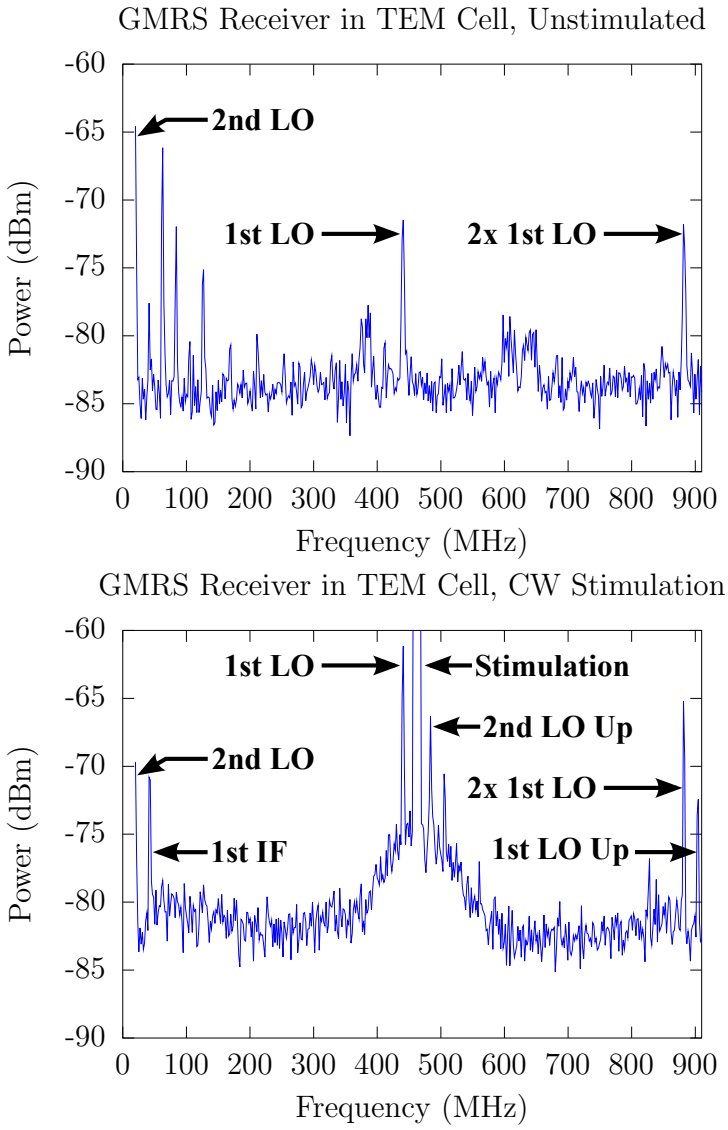

Figure 2.2: A comparison of unstimulated and stimulated emissions. Observe that the 440 MHz local oscillator, labeled "1st LO," is present in both captures, and that the 21.4 MHz ("1st IF") and 903 MHz ("1st LO Up") mixer outputs are only present in the stimulated case.

easy to identify since they require a stimulation signal and will always vary with respect to the stimulation.

GMRS radio receivers have identifiable local oscillator, intermediate frequency, and up-mixing emissions. Consider the different unintended emissions in Figure 2.2, which are enumerated in Table 2.1. f_{LO} is a signal that is both always present and very close to f_{RF}, making it most likely a local oscillator signal. f_{IF} and f_H are only present when the radio is stimulated, making them possible mixer outputs. Comparing the estimated frequency of each emissions signal, it is clear that $f_{IF} \approx f_{RF} - f_{LO}$ and $f_H \approx f_{RF} + f_{LO}$. Since the measured emissions satisfy (2.3) and (2.4), they follow the design rules for a superheterodyne receiver. Thus, f_{LO} and f_{IF} are the receiver's operating frequencies.

In the process of generating the above mathematically-required signals, GMRS receivers may also generate other, secondary signals that become unintended emissions. In Table 2.1, $2f_{LO}$ and f_{H_2} are examples of secondary emissions. High frequency oscillators often have second harmonics, and the $2f_{LO}$ emissions are just such a signal. The f_{H_2} emissions are the result of the second-stage LO mixing with the stimulation signal. Since there is no reason for the receiver to mix these signals, this signal is probably the result of poor electromagnetic isolation. While the secondary emissions may be useful, they are not mathematically guaranteed to exist, and it is possible to construct a superheterodyne receiver that does not generate them.

2.1.2. Time Domain Analysis. After determining the radios' operating frequencies, the unintended emissions were analyzed in the time domain. The emissions were sampled with an Ettus Research Universal Software Radio Peripheral (USRP), a software-defined radio which can both transmit and receive arbitrary radio signals. Unlike traditional oscilloscopes, which are limited by their memory depth, the USRP can record captures of nearly unlimited length. A more comprehensive overview of software-defined radio is given in Appendix 5. The USRP's frequency

span is quite small [21], and thus it is necessary to know the emissions' carrier frequency in advance.

GMRS receivers essentially only have two unique emissions signals. Consider the identified emissions frequencies in Table 2.1. All emissions that do not react to a stimulation are local oscillator signals, and all signals that react to a stimulation are mixer products. Since all signals of the same type contain the same information, it suffices to record one of each. As a matter of convenience, f_{LO} was selected for unstimulated emissions and f_H for stimulated emissions.

In order to determine if the f_H emissions originate from the radio's mixer, as postulated, several GMRS radios were tested with a stimulation signal. A repeating 5 kHz, 1024 ms linear frequency modulated (FM) chirp was up-mixed and transmitted to a nearby GMRS receiver. The transmitted signal's power was less than 200 mW, which is less than the radiated power of most GMRS radio transmitters. The frequency modulation used a maximum carrier deviation of $\Delta f = 5$ kHz, which is the same standard mandated for GMRS transmitters [22]. A USRP, placed in close proximity to the radio receiver, recorded the f_H emissions. In order to ensure that

Table 2.1: Identifiable Emissions Frequencies from Figure 2.2, $f_{RF} \approx 462$ MHz

Name	Frequency Estimate (MHz)	Changes when Stimulated	Description
f_{LO_2}	20.94	No	2nd Local Oscillator
f_{IF}	21.4	Yes	1st Intermediate Frequency
f_{LO}	441.0	No	1st Local Oscillator
f_{H_2}	483.5	Yes	2nd LO Up-mixing
$2f_{LO}$	882.0	No	Local Osc. Harmonic
f_H	903.0	Yes	1st LO Up-mixing

the USRP was not simply detecting a harmonic of the stimulation signal, a control capture was taken with no GMRS radio present.

As predicted, GMRS receivers have stimulated emissions at f_H, and these emissions are an up-mixed version of the original radio signal. The spectrogram of the emissions near f_H, shown in Figure 2.3, clearly indicates the presence of the original stimulation signal. The complex envelope increases from 0 Hz to 5 kHz over a period of 1024 ms, which matches the original stimulation signal.

A second measurement was taken using a different GMRS radio and a 1 kHz, pure-tone FM sinusoid. The emissions, shown in Figure 2.4, contain peaks that are characteristic of an FM sinusoid. At close range, It is possible to demodulate the emissions and recover the original tone. Other tests, not detailed here, indicate that it is possible to achieve a similar effect with arbitrary FM signals. The gaps in the emissions in Figure 2.3 and Figure 2.4 are caused by the local oscillator cycling on and off as it searches for a signal—a further validation that these emissions are caused by up-mixing in the radio.

GMRS radios periodically deactivate their local oscillators when no signal is detected. In order to quantify how the stimulation signal affects the emissions, the radio was placed in an RF-shielded environment, and the local oscillator emissions were recorded. Figure 2.5 shows the AM demodulation of one such recording. The reason for this response is explained below.

Since GMRS radios are intended for intermittent use and operate on shared spectrum, they incorporate squelch detectors to reject unwanted signals. Squelch detectors prevent unwanted audio output by muting the radio's speakers unless certain conditions are met. The first detector, carrier squelch, uses an energy detector to determine if a narrowband radio signal is present on the channel's carrier frequency. Because this channel may be shared among many users, receivers may also use tone

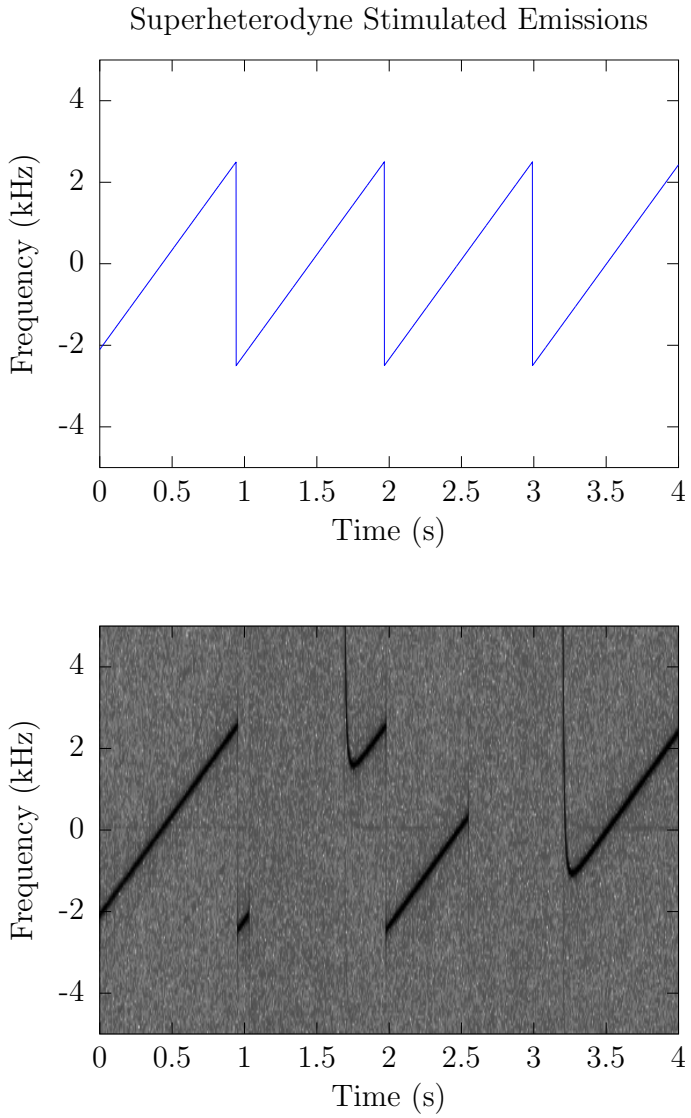

Figure 2.3: Spectrogram of up-mixing emissions. These f_H emissions are from a GMRS receiver, measured using the USRP. A GMRS receiver was stimulated with a repeating 5 kHz, 1024 ms linear FM chirp (top). The original stimulation signal is clearly visible in the emissions (bottom). The gaps in the signal are caused by the local oscillator's duty cycle.

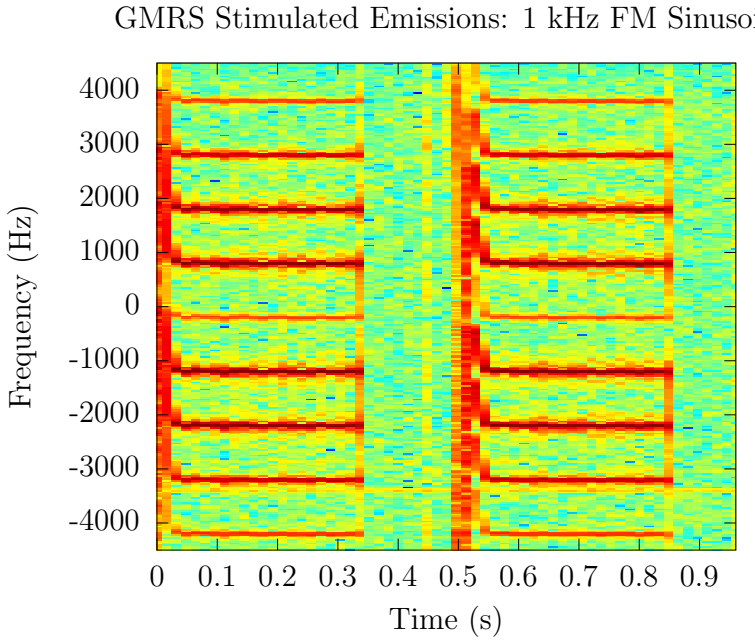

Figure 2.4: Spectrogram of up-mixing emissions from a second GMRS receiver model. The radio was stimulated with a 1 kHz frequency-modulated sinusoid, and the stimulation signal is visible in the emissions. It is possible to demodulate the emissions and recover the original tone.

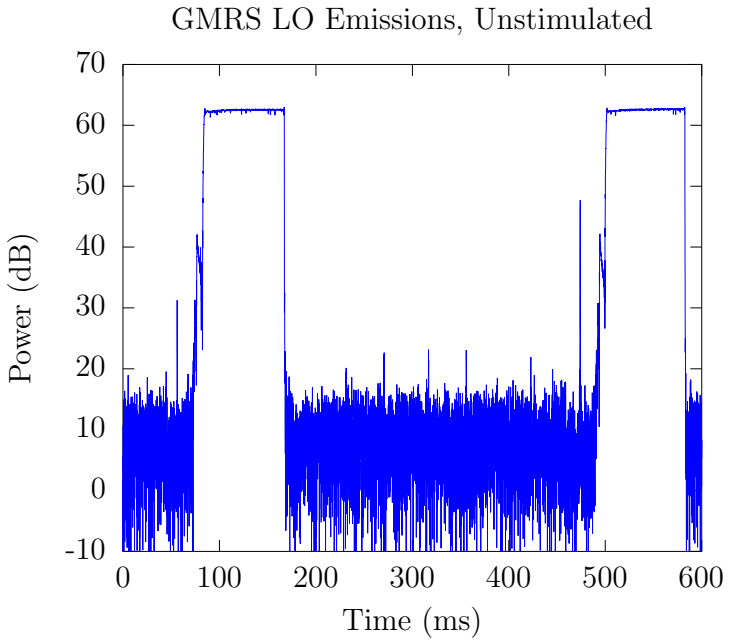

Figure 2.5: Magnitude of local oscillator emissions when the radio was not stimulated. Measured with the USRP.

(or code) squelch to suppress unwanted calls. Both detectors must be satisfied before the receiver un-mutes the speaker and plays back the incoming transmission.

Under this arrangement, the squelch detectors can be in one of three possible states. Since the squelch detectors operate in series, it is possible to have no detectors satisfied (S_0), just the carrier detector satisfied (S_1), or both the carrier and the tone detectors satisfied (S_2). The tone detector is optional and can be disabled by the radio's operator, and in this case it is always satisfied. Each state may have different unintended emissions, making it important to test each of them.

To investigate how the radio's squelch detectors affect its unintended emissions, the receiver was stimulated with a continuous wave (CW) signal, and the f_{LO} emissions were measured as before. S_1 was tested by enabling the tone detector. Since the CW stimulation was a narrowband signal that lacked any frequency modulation, it satisfied the carrier detector but not the tone detector. The tone detector was disabled to test S_2, and since the stimulation satisfied both detectors, the radio handled it like an incoming call.

According to the above test, GMRS radios deactivate their local oscillators whenever possible. If a receiver does not detect an incoming call (states S_0 and S_1), it occasionally activates its LO to poll the channel for a signal of interest. If the squelch detectors are not satisfied, the radio deactivates its LO. If the squelch detectors are satisfied, the radio enters state S_2, and the local oscillators are kept continuously active in order to down-mix the entire signal.

The results of this test procedure, for one GMRS receiver, are enumerated in Table 2.2, which shows the length of time that the local oscillator is active and the LO duty cycle. While the exact timing varies for different stimulation signals, the duty cycle is always much higher when the radio is in state S_1 than when it is in S_0. Since a receiver can only have f_H emissions when its LO is active, this behavior is clearly responsible for the gaps in Figure 2.3. The duty cycle will periodically

interrupt the radio's emissions, making it is important to consider this effect when designing a radio receiver detector.

2.1.3. Frequency Selection. In order to design a robust radio receiver detector, it is necessary to select emissions frequencies that are easy to detect. Time domain analysis shows that GMRS receivers have two different emissions signals—those that always exist (unstimulated) and those that are caused by a stimulation. Five distinct models of GMRS radios, from different manufacturers, were tested to check the validity of this assumption. To design an effective detector, only frequencies that exist in all studied GMRS receivers were selected.

All superheterodyne receivers are mathematically required to have an f_{LO}, an f_{IF}, and an f_H frequency. These signals can theoretically be of any frequencies that satisfy (2.2), and each superheterodyne receiver tested has observable emissions at these frequencies. Receivers may have unwanted harmonic signals, such as the $2f_{LO}$ component in Figure 2.2, but these signals are not required by design and may not exist in all receivers. Thus, the receiver detector was designed to use f_{LO} when detecting unstimulated emissions and either f_{IF} or f_H when detecting stimulated emissions.

Although GMRS radios have several different emissions frequencies, the ones that radiate in the far-field are the most useful. Since higher frequencies do not

Table 2.2: Effect of Squelch Detectors on Local Oscillator Duty Cycle

State			
Name	Detectors Satisfied	Active (ms)	Duty Cycle (%)
S_0	None	87.5	21
S_1	Carrier	429.5	57
S_2	Carrier & Tone	N/A	100

require large antennas to radiate efficiently, the stimulated emissions detector shown here was designed to use the 903 MHz f_H emissions.

Efficient antennas require two parts, each with a size on the order of $\lambda/4$ or larger, where λ is the wavelength. According to this relationship, the f_{IF} emissions at 21.4 MHz require parts on the order of 3.5 m long to radiate efficiently. In contrast, the up-mixed emissions at 903 MHz only require parts on the order of cm, which is roughly the same size as the radio receiver's printed circuit board. Because of the size of the GMRS radio, it is expected that the f_H up-mixed emissions to radiate much more strongly in the far-field than the f_{IF} emissions.

2.2. DESIGNING THE RADIO DETECTORS

Two radio receiver detectors were designed using the knowledge gained from these experiments. The first detector uses the traditional approach, silently listening for the f_{LO} signal without transmitting a signal of its own, making it a passive detector. The second detector is an active, stimulated emissions detector that transmits a known signal and searches for this signal in the f_H emissions, similar to the detectors in [14,17]. Both detectors were implemented in GNU Radio, the companion software for the USRP, and operate on the received emissions in real-time. To ensure a fair comparison, both algorithms were designed to use a frequency span of 10 kHz and a sampling rate of 64 kHz, and both algorithms produce one output statistic from N input samples.

2.2.1. Periodogram Detector. The periodogram detector detects GMRS radios by searching for their sinusoidal f_{LO} emissions. An ideal periodogram detector computes

$$S_x(f) = \frac{1}{M}\left|\sum_{n=0}^{M-1} x(n)\exp(-j2\pi nf)\right|^2 \tag{2.5}$$

and compares each bin $S_x(f)$ with a pre-set threshold. The detector is satisfied if one or more bins exceed the threshold. When used in this manner, the standard periodogram is a minimum probability-of-error detector, but it is computationally inefficient to compute (2.5) directly [23]. Instead, the periodogram is approximated using the Fast Fourier Transform (FFT).

The detector approximates the periodogram using Welch's method. Since each LO activation is only 80 ms long (from Table 2.2), it is necessary to choose an FFT size that is small enough to ensure that each activation has multiple FFTs—otherwise, the periodogram averaging will be more harmful than helpful. An $M = 2048$ point FFT ensures that each activation has at least two FFTs. A Hamming window is used, with 50% overlap, to improve sensitivity.

Finally, the detector searches for peaks in the periodogram. Since local oscillator signals appear as peaks, each periodogram point is compared with a pre-set threshold. If at least one point exceeds the threshold, a detection occurs (see Figure 2.6).

Since this approach does not require the use of a stimulation signal, it is a good example of a passive radio detector, and it is the same approach used for detection in [15]. It is far from ideal, however, since the f_{LO} emissions are non-stationary, and the periodogram cannot remove noise that overlaps the emissions in the frequency domain.

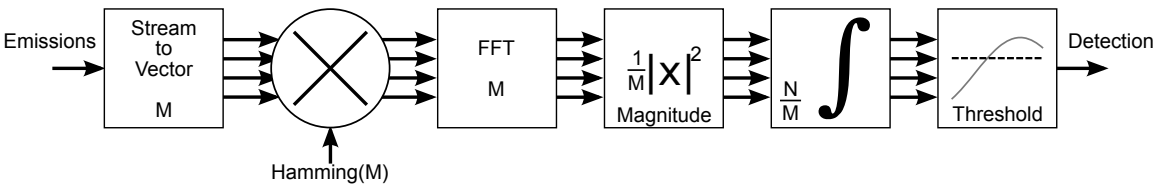

Figure 2.6: A passive detection algorithm using periodograms.

2.2.2. Matched Filter Detector: The Novel Approach. Since superheterodyne receivers up-mix and re-emit the signals they receive, it is possible to detect these receivers with stimulated emissions as proposed here. Since the stimulation and the emissions have identical complex envelopes, it is possible to use matched filtering to detect superheterodyne receivers. Matched filters, which are commonly used in radar signal processing, are the optimal linear filter for detecting any signal that is corrupted with additive white Gaussian noise (AWGN). For a stimulation signal $s[n]$ of length N, its matched filter $h[n]$ is

$$h[n] = s^*[N - n] \tag{2.6}$$

where s^* denotes the complex conjugate of s. The matched filter detector detects GMRS radios by transmitting the stimulation s and applying the matched filter h to the f_H emissions. While it is possible to use recorded emissions to detect devices [16], the stimulated emissions approach obviates the need for such recordings, since the filter can be generated directly from the stimulation signal. It is unnecessary to compile an exhaustive library of superheterodyne emissions—all superheterodyne receivers will have similar emissions.

In order to use matched filtering, it is necessary to select a stimulation signal s that is both compatible with the radio receiver and is easy to detect. In additive white Gaussian noise, a matched filter's performance depends only on the signal's energy—and not its waveform [24]. Thus, it is desirable for the emissions to have high power and long duration, but the matched filter imposes no additional constraints on s. The radio receiver itself is a more important factor in choosing a stimulation signal.

Stimulation signals that resemble radio calls produce higher-energy emissions. As shown in Table 2.2, if a GMRS receiver's carrier squelch is satisfied, then its local oscillator remains active for a longer period of time. This increases the average

energy of the emissions, making the receiver easier to detect. To satisfy the carrier squelch, the stimulation signal must resemble the same type of signal used by GMRS receivers. For maximum compatibility, s should conform to [22]—i.e., be a narrow-band frequency modulated signal with $\Delta f = 2.5$ kHz. In order to satisfy the squelch detector, the stimulation signal must be transmitted on the same channel that the GMRS receiver is tuned to.

Radio receivers have different intermediate frequencies, resulting in different f_H frequencies, and the inexpensive oscillators used in many consumer radios exhibit subtle fluctuations with temperature and power supply voltage. Since it is impossible to know f_H precisely, the received emissions will have considerable frequency ambiguity. While techniques exist to compensate for frequency drift, such as quadrature demodulation or phased-locked loops, each of these techniques require high signal-to-noise ratio (SNR)—and the emissions are a very weak signal. Thus, s should be a signal that match-filters well even when it is frequency-shifted.

One signal that meets the above criteria is a linear frequency modulated (LFM) chirp. LFM chirps are generated by using a linear ramp signal as the input to a continuous-phase frequency modulator. Applying a small frequency shift to an LFM chirp is roughly equivalent to applying a small time shift, and this property causes LFM chirps to match filter effectively even when frequency-shifted [25]. The chirp bandwidth must be 5 kHz, to conform to the radio's expected input, and the amplitude should be as high as possible, making the duration the only tunable parameter.

It is worth noting that the local oscillator's duty cycle does not impose a hard upper bound on the stimulation duration. From Table 2.2, the radio's local oscillator is only active for 400 ms at a time. When it is inactive the matched filter accumulates only noise. The amount of noise accumulated, however, is a function of the duty cycle and not the stimulation duration. It is possible to use a chirp stimulation that extends across multiple activations, and while the entire chirp is not received, the parts that

are received still correlate. With the above in mind, our matched filter detector uses a high-energy LFM chirp that is $N = 2^{16}$ samples long at its operating sampling rate of 64 kHz, giving it a period of roughly 1024 ms. The stimulation signal is shown in Figure 2.3.

The matched filter detector transmits this LFM chirp to the radio and applies the matched filter to the received f_H emissions. The matched filter is a finite impulse response (FIR) filter, and thus it can be applied quickly using FFT techniques. Since the matched filter detector, shown in Figure 2.7, knows that each chirp is N samples long, it searches for a maximum of one match every N samples. The output is then compared with a threshold detector: if the matched filter's output exceeds the threshold, a detection occurs. In order to determine how many chirps have been received recently, an integrator counts the number of detections that have occurred within the past few seconds.

2.3. THEORETICAL PERFORMANCE

Each detector's theoretical performance was evaluated using artificial GMRS radio emissions. Due to RF propagation, antenna, receiver sensitivity, and emissions power differences, it is challenging to fairly compare these two algorithms in an experimental setting. The detectors use two different emissions frequencies, f_{LO} and f_H, that radiate in a different fashion, with different power levels. This invariably results in different signal-to-noise ratios (SNR) at the receiver, giving one algorithm an

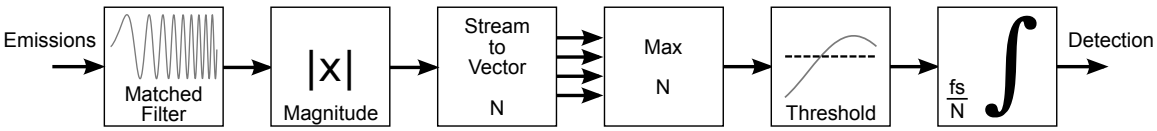

Figure 2.7: A stimulated emissions detection algorithm using matched filters.

advantage over the other. To compare these detectors under equal-SNR conditions, artificial emissions were generated based on experimental data.

2.3.1. Emulating GMRS Emissions. The emissions simulator generates two sets of emissions: f_{LO} emissions and f_H emissions. The simulated f_{LO} emissions start as a constant-amplitude sine wave, and the f_H emissions start as a perfect-match LFM chirp. Both signals start with exactly identical RMS powers (0 dBW). Prior to testing, the signals are time-limited, frequency-shifted, and corrupted with additive white Gaussian noise.

GMRS radios have different local oscillator duty cycles when they are unstimulated (state S_0) and when they are stimulated (state S_1). To emulate this effect, the ideal emissions are multiplied with square waves with the same duty cycles that are listed in Table 2.2. The square wave has a value of 1 when the LO is "on" and 0 when the LO is "off," windowing the emissions in the time domain. Finally, the emissions are subjected to channel effects.

The artificial emissions are corrupted with a small frequency shift and additive noise. Since the exact emissions frequencies can never be known in advance, both emissions are subjected to a small (1 kHz) linear frequency shift. After shifting the emissions, both the f_{LO} and the f_H signals are corrupted by the exact same additive white Gaussian noise sequence. The amount of noise was varied to produce SNRs from 0 dB to -35 dB. The artificial emissions and the generated noise signal are then saved for testing.

2.3.2. Quantitative Results. The artificial emissions were used to compare the efficacy of both detectors in terms of their Receiver Operating Characteristic (ROC) curves. To test the case where a radio is present, the artificial f_{LO} emissions were run through the periodogram detector, and the artificial f_H emissions were run through the matched filter detector. To test the case where no radio is present, both detectors were run using the generated noise signal as input. Each true positive (p_{true}),

false positive (p_{false}), true negative (n_{true}), and false negative (n_{false}) was counted, and the test was repeated for many different detector thresholds.

For each test, the false positive rate (fpr) and true positive rate (tpr) were calculated as

$$fpr = \frac{p_{\text{false}}}{p_{\text{false}} + n_{\text{true}}} \tag{2.7}$$

$$tpr = \frac{p_{\text{true}}}{p_{\text{true}} + n_{\text{false}}} \tag{2.8}$$

When plotted, the false positive and true positive rates represent the ROC curve. While both algorithms performed equally well for high SNRs, the difference became more pronounced at lower SNRs.

Figure 2.8 shows the ROC curves for both detectors for various signal-to-noise ratios. Since the matched filter detector has more area under each curve than the periodogram detector, it more accurately determines whether or not a radio is present. Since the matched filter detector outperforms the periodogram detector under high-noise conditions, the stimulated emissions approach is a quantitative improvement over existing algorithms for detecting radio receivers.

It may be possible to further improve the performance of both the active and passive detectors. Wavelets are widely used in chirp radar applications [26], and their high time/frequency resolution may assist in the location of radio receivers. Additionally, new statistical techniques can increase the sensitivity of periodogram detectors. By comparing the periodogram with a probability distribution, rather than a threshold, it is possible to reliably determine if a sinusoidal signal is present—without the need to set a threshold [27].

2.3.3. Qualitative Results. In addition to the quantitative gains, the matched filter detector offers a qualitative reduction in false positives. High-frequency oscillators are not unique to radio receivers. Many other types of circuits—such as

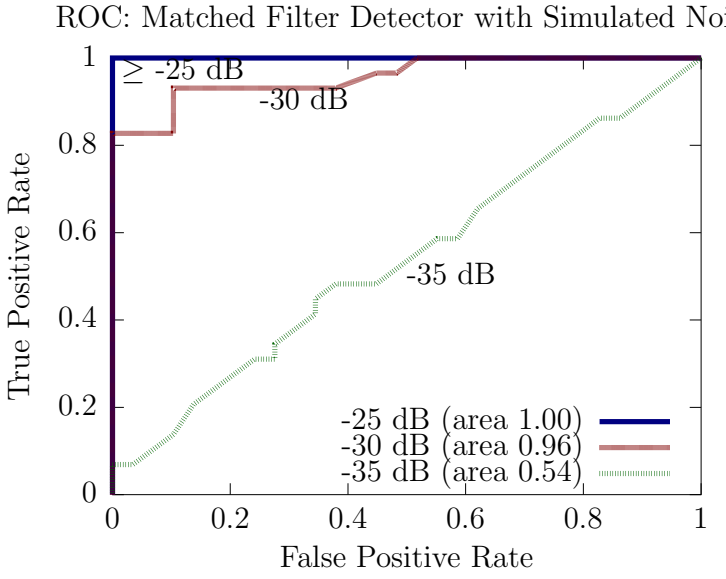

(a) Matched Filter Detector

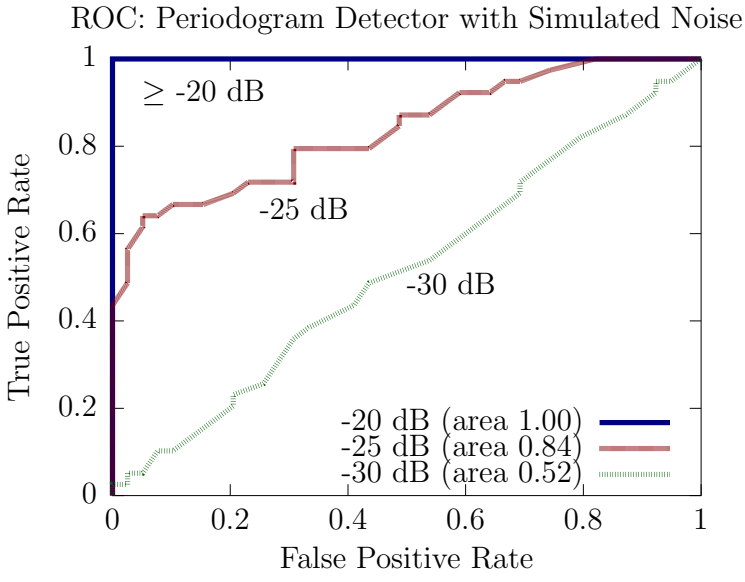

(b) Periodogram Detector

Figure 2.8: Receiver Operating Characteristics of both the matched filter detector and the periodogram detector. The matched filter detector significantly outperforms the periodogram detector when the signal-to-noise ratio is -25 dB or less.

digital logic systems—may incorporate them. If such a device has high frequency emissions near f_{LO}, then it may cause a false positive on a periodogram detector. Conversely, the matched filter detector provides assurances that the detected device is a superheterodyne receiver, since only a superheterodyne receiver will react to the stimulation as shown here. For applications that depend on the reliable detection of radio receivers in the presence of other electronics, the stimulated emissions approach is clearly superior.

2.4. CONCLUSION

The proposed stimulated emissions approach outperforms existing methods for detecting superheterodyne receivers. Measurements of unintended emissions demonstrate that two-way superheterodyne radios have higher-energy emissions when stimulated, facilitating accurate detection. Key emissions are shown to have an identical complex envelope to the stimulation signal, making it possible to detect receivers using a matched filter. Theoretical performance testing affirms that, under low SNR conditions, the matched filter detector offers a 5–10 dB performance gain over passive techniques. While an experimental performance evaluation is necessary, these results indicate that the stimulated emissions approach is a useful technique for reliably detecting superheterodyne radio receivers.

3. LOCATING SUPERHETERODYNE RECEIVERS

As the preceding sections demonstrate, one strategy for mitigating explosive threats is to detect radio receivers. Previous work has shown that radio receivers have unintended electromagnetic emissions [15,16]. These unintended radio frequency (RF) emissions are present any time the receiver is powered on and cannot be easily eliminated with shielding. They are, however, limited in power and may be masked by stronger signals from intentional radiators, making them difficult to detect. In many cases, it is possible to improve detection by using *stimulated emissions* techniques.

Stimulated emissions is a well-known phenomenon [14, 17] that can occur in a variety of electronic devices. Certain types of devices—most notably, radio receivers—are inherently sensitive to ambient RF signals. By transmitting a weak stimulation signal, it is possible to alter the internal state of the device. The change in state causes a change in the device's unintended emissions. A stimulated emissions detector, such as the one depicted in Figure 3.1, can offer improved sensitivity and selectivity over passive detectors [12], since detection uses specific information about the emissions. For the sake of clarity, the superheterodyne receiver that the system is attempting to locate is referred to herein as the *target device*.

Knowing the position of the target device, as well as whether or not the device is moving, would help confirm the presence of an explosive threat. The system developed in [12] to detect radio receivers is merely a proximity detector. It can detect the presence of a target device, but it cannot determine its location. RF sources can be located by measuring the received signal strength, angle of arrival (AoA), or time of arrival (ToA) of the radio signal. Any of these techniques can be applied to locate unintentional radiators.

Received-signal-strength and angle-of-arrival algorithms are ill-suited to this particular application. Received-signal-strength methods make the implicit assumption that the source signal radiates isotropically [28]. This assumption does not hold for unintended emissions, which do not have purpose-built isotropic antennas. Angle-of-arrival techniques require directional antennas [29] or large antenna arrays [30], which increase the size and expense of the system. Subspace techniques such as Estimation of Signal Parameters Via Rotational Invariance Techniques (ESPRIT) offer high-resolution AoA estimation [31], but they are seldom realized in hardware and are particularly sensitive to multipath [32].

ToA techniques are frequently used in radar and radio-navigation systems. In the Global Positioning System (GPS), receivers determine their position by measuring the ToA of synchronized signals from multiple sources [33]. This technique is known as time difference of arrival (TDoA). The accuracy of these radio-navigation systems is dependent, in part, on the accuracy of the TDoA measurements. In order to be of practical use, a radio receiver locator must make highly accurate ToA measurements.

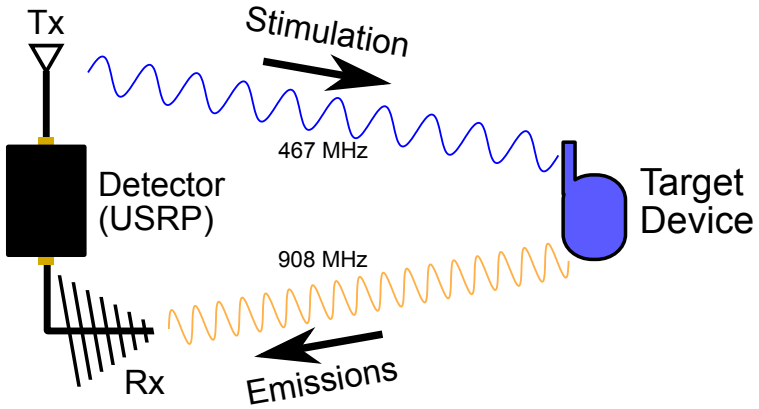

Figure 3.1: The stimulated emissions detection process. A stimulated emissions detector alters the unintended emissions in a predictable manner. The modified emissions radiate back into the environment, where they are detected. The frequencies given above are an example only.

A ToA-based method is developed in the following paper for determining the range to non-cooperative radio receivers using stimulated emissions. The method extends the previous stimulated detection approach, which could not locate radio receivers, to allow ToA measurement. The theoretical accuracy of the ToA estimates is determined using near-field measurements. A radar-like technique is used to locate consumer radio receivers in a real RF propagation environment. Experimental performance tests indicate that it is possible to reliably and accurately locate superheterodyne receivers.

3.1. METHODS

The crucial factor impacting the accuracy of a time-of-arrival estimation system is, as the subsequent sections will demonstrate, the available bandwidth. Existing stimulated emissions techniques, which are briefly reviewed, do not take the bandwidth limitations of the target device into account. The bandwidth of a General Mobile Radio Service receiver is measured, and an appropriate time-of-arrival technique is developed based on the characteristics of the stimulated emissions. The hardware implementation of this technique, which is based on chirp radar, is also discussed.

3.1.1. Wideband Stimulated Emissions. In [12], it was demonstrated that superheterodyne receivers have stimulated emissions that are a frequency-translated copy of the stimulation signal. Superheterodyne receivers, such as the one shown in Figure 3.2, use mixers to perform frequency translation [34]. In this receiver, the RF signal is shifted in frequency to a fixed intermediate frequency, f_{IF}, by selecting the local oscillator frequency, f_{LO}, such that

$$f_{IF} = f_{RF} - f_{LO}. \tag{3.1}$$

By the modulation theorem, the mixer also creates an up-mixing component, f_H, at

$$f_H = f_{RF} + f_{LO}. \tag{3.2}$$

It has been shown that superheterodyne receivers can be detected by transmitting an arbitrary stimulation signal at f_{RF} and searching for the f_H emissions with a correlator. In order to locate the receiver, the round-trip time of the stimulated emissions must also be accurately measured.

Others have shown that the accuracy of time-of-arrival measurements depends on the signal-to-noise ratio (SNR) and waveform of the received signal [35]. While it is difficult to obtain a closed-form expression of accuracy for arbitrary signals, closed-form solutions for specific radar signals exist. As given in [35], the accuracy of a linear, frequency-modulated (LFM) chirp is

$$\delta R_{\text{ideal}} = \frac{c\sqrt{3}}{2\pi B(2E/N_0)^{1/2}}, \tag{3.3}$$

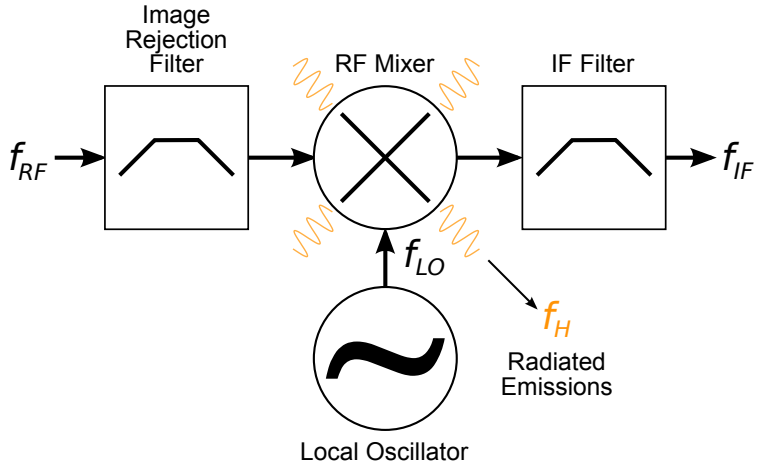

Figure 3.2: A superheterodyne front-end which uses low-side injection. The radiated emissions originate from the RF mixer.

where δR_{ideal} is the root mean square (RMS) position error, c is the speed of light, B is the chirp bandwidth, and E/N_0 is the SNR in linear units. The RMS error represents the average-case, absolute position error.

From (3.3), the error δR_{ideal} decreases proportionally with respect to the bandwidth used—but only with the square root of the SNR. This property makes it highly advantageous to use wideband signals for time of arrival-based location. The narrowband, $B = 5$ kHz chirps used in [12] have an error that is too large to be of practical use for realistic SNRs. Additional bandwidth is required to perform meaningful time of arrival-based location.

While superheterodyne receivers were previously detected using narrowband stimulations, which were the width of a single voice channel, superheterodyne front-ends are sensitive to a much wider range of frequencies. Consider the simplified receiver front-end in Figure 3.2. The mixer, which produces the f_H stimulated emissions, must be sensitive to the entire range of frequencies to which the radio can tune. The bandwidth of the signal that can enter the mixer is limited only by the resonance of the antenna and the image rejection filter.

The image rejection filter is designed to eliminate frequencies which are far outside of the receiver's tuning range. Superheterodyne receivers select two channels at once, making it necessary to eliminate one of them with a filter. The unwanted channel, known as the image frequency, is located at

$$f_{\text{image}} = f_{RF} - 2f_{IF} \tag{3.4}$$

for low-side injection receivers. For receivers using the popular $f_{IF} = 21$ MHz intermediate frequency, the image frequency is $2f_{IF} = 42$ MHz away from the RF channel. Since the frequency separation is relatively large, the image rejection filter

can—but does not necessarily—have a pass band that is much wider than the range of frequencies to which the device can tune.

Receivers that use such image rejection filters, with wider-than-necessary pass bands, can have a stimulated emission's bandwidth which far exceeds their tuning range. This theory is important, as higher bandwidths yield more precise position measurements. In order to determine the usable bandwidth of real-world devices, a number of consumer superheterodyne receivers were selected for testing in a controlled environment.

3.1.2. Bandwidth Measurements. Initial testing was performed using General Mobile Radio Service (GMRS) radios. GMRS radios are typical consumer superheterodyne receivers. GMRS is a low-power land-mobile radio service, which operates on frequencies in the 460 MHz range using analog frequency modulation. Since superheterodyne radio receivers have been available for many years [36, 37], most commercially-available radio receivers use very similar designs, and results with the tested receivers are easily generalizable to other devices and services.

The stimulated emissions bandwidth that can be used with a GMRS receiver was determined using frequency-domain measurements. While a superheterodyne receiver is not a strictly linear system, the principal non-linearity—the mixer's frequency shift—is known from (3.2). By transmitting a stimulation signal on f_{RF} and measuring the corresponding stimulated emissions on f_H, it is possible to determine the linearized system's frequency response. To improve isolation from ambient RF signals, these measurements were conducted in an enclosed near-field environment.

A GMRS receiver was placed in a transverse electromagnetic (TEM) cell, and its stimulated response was measured. The device under test was a double-conversion superheterodyne receiver with an intermediate frequency of $f_{IF} = 21.4$ MHz. The stimulated response was determined using a swept-sine technique similar to that

in [38]. A signal generator was used to produce a swept sinusoidal stimulation from 450 – 560 MHz. The stimulated emissions were measured using a spectrum analyzer.

The stimulated response is shown in Figure 3.3. The results indicate that the GMRS receiver will generate stimulated emissions over a bandwidth of approximately 16 MHz. This measurement is significant since the GMRS receiver is only designed to receive a 175 kHz-wide band. The receiver's response is dominated by the pass-band properties of the image rejection filter. The emissions are within 3 dB of the peak power for stimulation frequencies of 455.853 MHz – 478.893 MHz. Outside of this band, the image rejection filter attenuates the stimulation signal, limiting the bandwidth of the emissions.

Results show that sufficient bandwidth exists for high-resolution location. Although sufficient bandwidth is available, other factors may impact or impede far-field distance measurements.

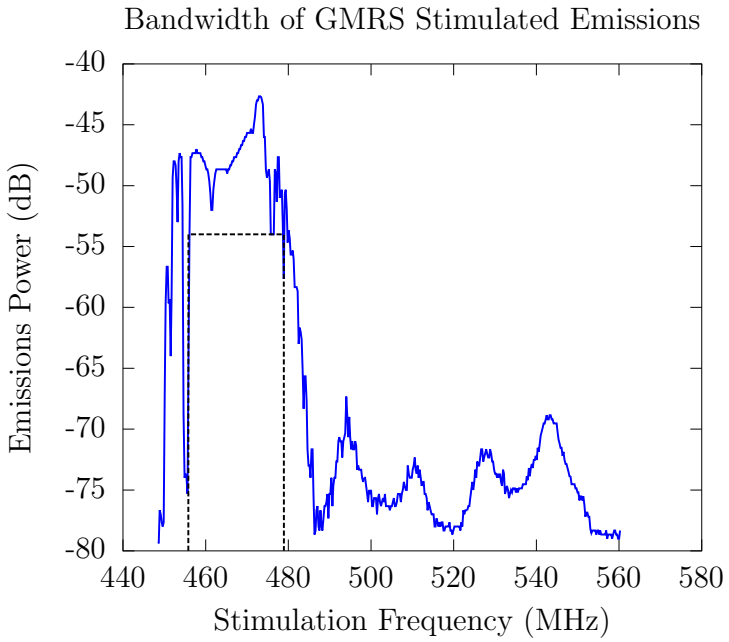

Figure 3.3: Stimulated emissions of a GMRS receiver. The 3 dB bandwidth, measured relative to the power at GMRS channel four (462.6375 MHz) is indicated on the plot as a dashed line.

3.1.3. Time of Arrival Method. Continuous-wave radar concepts can be applied to locate radio receivers. Pulse-radar techniques would not work well since superheterodyne receivers frequently incorporate low-noise amplifiers which compress the dynamic range of the received signal and, by extension, the stimulated emissions [39]. Signals with nearly-constant power, such as continuous-wave signals, can deliver a higher average power through these amplifiers [40].

Frequency-modulated continuous wave (FMCW) radar methods are well-suited to detecting superheterodyne receivers. FMCW radar uses a swept-sine signal to achieve the bandwidth required for accurate ranging. Although a variety of FMCW signals have been studied, efficient techniques exist for processing linear FM chirps. As described in [41, 42], and elsewhere, delaying an LFM chirp in time is equivalent to shifting it in frequency. The difference between the transmitted frequency and the received frequency determines the range information.

The frequency difference, which is often referred to as the beat frequency, is given by the relationship

$$f_b = \frac{\tau B}{T}, \tag{3.5}$$

where f_b is the beat frequency, τ is the time delay, and T is the chirp period [41]. This relationship makes it possible to implement FMCW radar using mixers. In order to determine the beat frequency, the received echoes are mixed with the complex conjugate of the transmitted chirp signal. The product signal contains, among other periodic terms, the beat frequency signal. This reduces the range estimation problem to a frequency estimation problem.

The Fast Fourier Transform (FFT) is a numerically efficient estimate of the beat frequency. A one-dimensional FFT estimates range, and a two-dimensional FFT estimates range and doppler shift simultaneously [40,43]. FFTs from successive chirp periods are typically averaged together using periodogram techniques. Due to the

oscillator drift between the radar and the target device, the "doppler" frequency has a different meaning in this application compared to traditional radar.

The major difference between conventional radar and the technique used here is that the return signal is not a reflection; it is modified emissions from the target device. Traditional radar has a strictly linear echo path, and any frequency shift is the result of the doppler effect. This is not the case for stimulated emissions, which are shifted in frequency by the target device's local oscillator. In practice, the local oscillator frequency is unknown and may drift somewhat over time. The precise stimulated emissions frequency is, by extension, unknown, but it can be estimated using doppler processing techniques.

Doppler shift is usually modeled as a linear frequency shift between the transmitted and received radar signals [44]. Techniques for estimating doppler can thus estimate the frequency shift between the radar and the target device. This estimate is useful for separating multiple targets, which tend to have slightly different local oscillator (LO) frequencies. The "doppler" estimate is also necessary to ensure that the mutual oscillator drift between the radar and the target device does not result in range ambiguity.

Due to the relationship between a time shift and a chirp frequency shift, excessive frequency shift will also change the estimated range. From [40], the maximum unambiguous frequency shift ΔD is

$$\Delta D = \frac{1}{T}. \tag{3.6}$$

If either the radar's oscillator or the target's oscillator drift in frequency by more than ΔD, the estimated range will change. While longer chirps are preferable, since they deliver more energy per chirp, the chirp period T must be small enough to avoid this ambiguity.

The mixer implementation quantizes all range estimates into discrete range bins. As derived in [45], the range resolution for frequency-modulated sawtooth waveforms is

$$\Delta R \approx \frac{Tc}{2B}\sqrt{\left(\frac{1}{T-t_d}\right)^2 + \Delta f_r^2}, \tag{3.7}$$

where t_d is the transition time between chirps, and Δf_r is the frequency resolution of the receiver. Assuming a sufficiently fine-grained frequency estimate ($\Delta f_r = 0$) and instantaneous transitions ($t_d = 0$), this simplifies to

$$\Delta R \approx \frac{c}{2B}. \tag{3.8}$$

The size of the range bins is thus a function of bandwidth. With $B = 16$ MHz of bandwidth, each range bin is $\Delta R \approx 9.4$ m wide.

3.1.4. Hardware Realization. The radio receiver's near-field bandwidth is not, by itself, sufficient to determine the performance of a ToA range estimation system. RF propagation, such as antenna resonance and multipath, can have a substantial impact on the stimulated emissions in the far-field. Oscillator imperfections can result in frequency drift and phase noise, reducing resolution [40]. To test the effects of these factors, a continuous-wave radar was designed and implemented in hardware.

An FMCW radar-like system was designed to implement the stimulated emissions process described in Figure 3.1 and in the last section. Existing FMCW radars are designed to detect linear echoes from reflective surfaces. They are ill-suited for detecting unintended emissions, which may have very different stimulation and emissions frequencies ($f_{RF} \neq f_H$). This design requirement necessitates the development of a modified FMCW radar with greater frequency agility.

The stimulated emissions radar uses a Universal Software Radio Peripheral (USRP) to perform high-speed signal processing. The USRP is a software-defined

radio that enables personal computers (PC) to transmit and receive radio signals. A block diagram of the radar system is presented in Figure 3.4. Additional information about the USRP system and software-defined radio in general is given in Appendix 5.

The USRP incorporates two independently-tuned daughtercards for RF frontends. One card transmits the stimulation signal at f_{RF}, and the other receives the f_H stimulated emissions. The receiver uses a yagi antenna for extra directionality, additional analog filtering to attenuate the transmitted signal, and external low-noise amplifiers to increase the SNR. The USRP's field-programmable gate array (FPGA) performs the high-speed radio and radar signal processing.

The USRP connects to its host PC through the Universal Serial Bus (USB) protocol. This connection has a maximum transfer rate of 8 MSa/s [21], which is too slow to accommodate wideband chirp radar signals and satisfy real-time performance requirements. To reduce the required throughput, a custom FPGA bitstream performs the chirp and de-chirp operations. The radar frontend uses a sawtooth waveform with an adjustable period and bandwidth.

The beat frequency signal is filtered, decimated, and transferred to the host PC. The resulting signal has an integer number of samples per chirp, N. A range-Doppler periodogram, similar to that in [43, 46], estimates range and frequency shift.

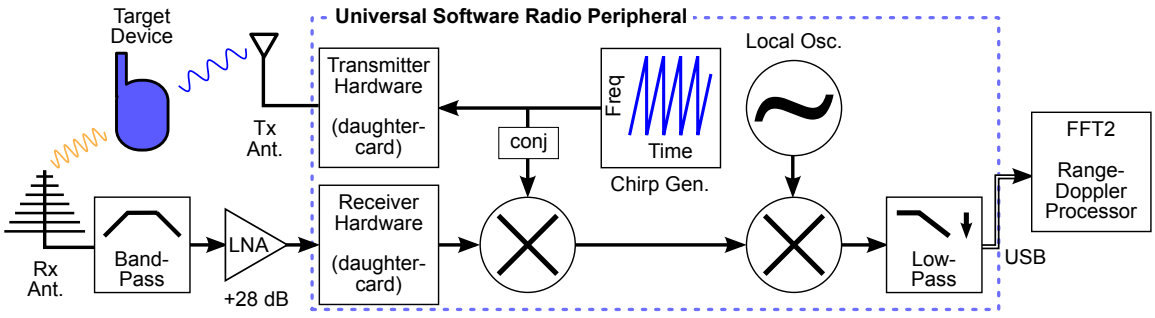

Figure 3.4: Hardware realization of the stimulated emissions radar. A linear FM chirp generator was added to the USRP's FPGA. The de-chirped emissions are down-mixed, decimated, and output to the host PC for further processing.

To compute the periodogram, N chirps are accumulated, as column vectors, into an $N \times N$ matrix. A Hamming window is applied to the matrix to reduce the effects of the inter-chirp transitions. The two-dimensional FFT ($2N \times 2N$ points) of the matrix is computed.

Multiple FFTs are averaged together, forming a two-dimensional range-doppler periodogram [47]. The target's range and frequency shift are estimated from the maximum of the periodogram. While more advanced frequency estimation [48] and tracking techniques are available, this estimate suffices for single-device tests. A simple post-processor improves the effectiveness of the range-doppler processor.

The RF front-end of the USRP used in these experiments is less than ideal for FMCW radar. Even with extra analog filtering, there is strong, in-system coupling between the transmitted stimulation and the received emissions. The coupling increases the received power of several different doppler frequencies. These spurious bands of energy make it necessary to estimate the noise floor of each doppler frequency individually.

The post-processor estimates the noise floor of each doppler frequency using its 20-quantile power—i.e., the power that only 20% of the cells are less than. The noise estimates are then used to equalize the power of all doppler shifts. This technique is a simple form of the constant false-alarm rate (CFAR) processor which is commonly used in radar systems [49].

The accuracy of the radar system was verified by using a long coaxial cable as a delay line. The radar transmitter was connected directly to the receiver via a 34.3 meter RG-58 cable. A frequency doubler was placed in the loop to mimic the frequency shift which occurs in a superheterodyne mixer. The radar made thirty range estimates over a 2.5 minute period, using both 16 MHz and 32 MHz of bandwidth. No drift or variance was observed in the range estimates. The USRP's range estimates (48.8 m) are reasonable given both its resolution and the velocity factor of

the coax. After validation testing, the stimulated emissions radar was used to locate superheterodyne receivers.

3.2. RESULTS

Field trials of the stimulated emissions radar were conducted using two different target devices at two different locations. The first device was the GMRS receiver from Section 3.1.2, which had approximately 16 MHz of usable bandwidth. The second device was a wideband radio scanner which had a tuning range of 420 – 470 MHz ($>$ 50 MHz bandwidth). Both devices were commercially-available superheterodyne receivers that were certified to comply with FCC radiated emissions limits. The GMRS receiver is a typical low-cost consumer receiver, while the wideband scanner is a higher-quality, more sensitive device. The range to these devices was determined using the USRP as previously described.

The chirp parameters were chosen such that the stimulated emissions bandwidth was identical for both devices. From Figure 3.3, a $B = 16$ MHz-wide chirp centered on $f_{\mathrm{RF}} = 467$ MHz will pass through the GMRS receiver. Two different tests, one outdoors and the other indoors, were conducted for each target device. Both tests used similar hardware configurations and an identical test procedure.

During each trial, the target device was carried by hand on a fixed path, first away from and then towards the radar unit. The target was kept in motion continuously during each trial, with an average velocity which varied from 0.85 m/s to 1.07 m/s.

In order to increase the SNR, the target device's squelch detector (see [12]) was disabled, forcing the receiver to be active continuously. The stimulated emissions radar tracked and estimated the range to the target device throughout the trial. A chirp period of $T = 0.8$ ms was chosen to allow for $\Delta D = 1.25$ kHz of unambiguous

frequency shift. Five seconds (1.6×10^6 samples) of stimulated emissions were used to make each range estimate.

The range estimates were compared to the known, true position of the device over time. Each trial included distances, in five meter increments, from five to fifty meters away from the radar unit. No outliers were discarded. This procedure was repeated a total of fifteen times, generating a total of thirty data points per range increment tested.

3.2.1. Indoor Test. The test was conducted in a hallway of a modern, three-story office building. The building's floors were constructed from reinforced concrete with rebar. Interior rooms are divided using drywall panels and solid wooden fire doors. The hallway had ceramic tile flooring and drop ceilings. This setup is not expected to "shield" the test environment from external noise.

The test results demonstrate that the stimulated emissions radar accurately determines the range to both devices. The range estimates for the two target devices are plotted in Figure 3.5 with standard deviation error bars. The mean range error is less than 5 m at each distance. The 95% confidence intervals, given for each distance in Table 3.1, indicate that the estimated means are representative of the system's true performance.

3.2.2. Outdoor Test. Outdoor testing was conducted in an isolated rural area, away from large buildings or metallic reflectors. In order to increase the SNR, a yagi antenna was added to the radar transmitter. As shown in Table 3.2, the accuracy of the radar improves under these conditions—the mean range error is less than 4 m. The effective maximum range outdoors is only 35 m, however.

Table 3.1: Indoor Test Results

	Est. Range (m)			
	GMRS		**Scanner**	
Range (m)	Mean	95% CI	Mean	95% CI
5	3.0	0.6	5.0	1.4
10	10.7	1.3	9.8	0.5
15	12.5	0.8	15.5	1.3
20	23.3	1.6	22.3	1.1
25	24.4	1.5	27.0	1.2
30	30.5	0.8	30.8	1.3
35	33.3	1.7	34.6	1.8
40	40.2	0.6	45.0	1.9
45	48.0	1.3	49.5	1.0
50	49.7	0.5	49.7	1.4

Table 3.2: Outdoor Test Results

	Est. Range (m)			
	GMRS		**Scanner**	
Range (m)	Mean	95% CI	Mean	95% CI
5	5.0	0.3	5.0	0.9
10	7.8	0.8	7.8	1.3
15	14.0	1.1	14.0	0.9
20	19.2	1.2	19.2	1.3
25	23.7	0.8	23.7	0.9
30	29.6	1.5	29.6	1.4
35	33.1	0.9	33.1	1.5
40	43.2	4.1	43.2	4.6

3.3. DISCUSSION

Wideband stimulated emissions is, demonstrably, an effective technique for locating superheterodyne receivers. An analysis of the system's accuracy, which is given below, indicates that the system has a reasonable noise performance which corresponds well to the theoretical model. While it is possible to locate radio receivers using wideband stimulated emissions, a number of important challenges remain. The target device introduces a number of limitations which can reduce the effectiveness of the system. Multipath can also pose a problem, particularly indoors. These

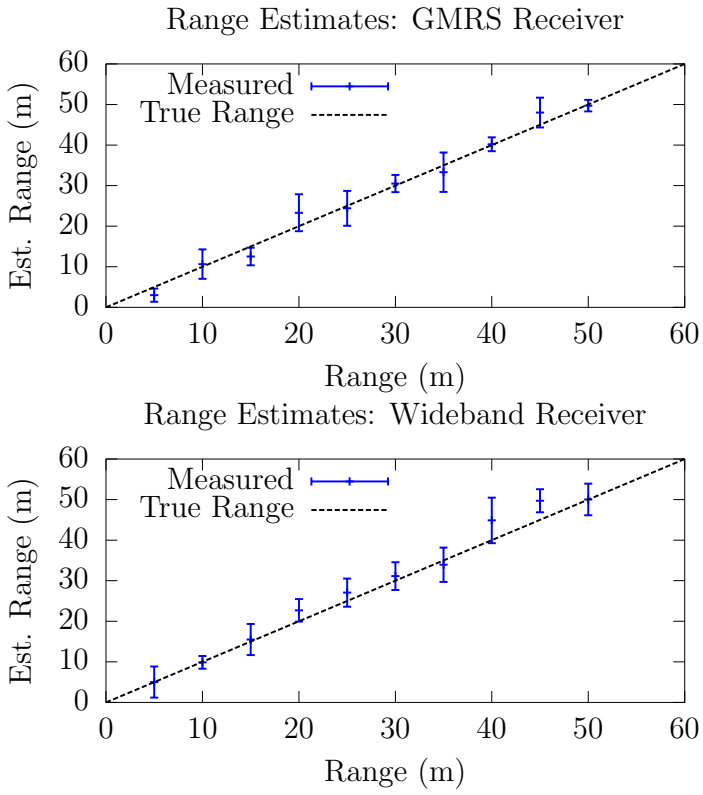

Figure 3.5: Indoor range estimates of the GMRS receiver and the wideband scanner. Each range estimate plotted above is the mean of thirty range measurements; estimates are plotted with standard deviation error bars. The true range is plotted, for reference, as a dashed line.

challenges, and potential strategies to mitigate their impact, are discussed in the following sections.

3.3.1. Analysis of Accuracy. The accuracy of a ToA system is traditionally measured using its root mean square error performance at various signal-to-noise ratios [35, 50, 51]. In order to quantify the accuracy, the experimental performance results shown in Table 3.1 and Table 3.2 were compared with the theoretical SNR performance equation (3.3). Controlling the SNR is difficult in an experimental setting, however, making it necessary to estimate the SNR from the data. The SNR of each range estimate of the outdoor tests was estimated from the peak-to-average power ratio of its range-doppler periodogram. In order to average a sufficient number of error terms, the SNRs were rounded to the nearest 5 dB, and the RMS position error was calculated for each SNR.

The experimental RMS errors ϵ obtained above were fit to the following simplified model of the measurement accuracy versus SNR:

$$\epsilon = \frac{\alpha_1}{(2E/N_0)^{1/2}} + \alpha_0 \tag{3.9}$$

where α_0 and α_1 are unknown constants determined by linear regression. As shown in Figure 3.6, results indicate that the radar's SNR performance can be predicted from the theoretical model (3.9) with a coefficient of determination of 0.976. For the distances tested, the RMS position error is strictly less than 5 m when the SNR is 15 dB or higher, which is reasonable given the available resolution. A similar analysis for the indoor test data indicates an RMS position error of less than 4 m for SNRs above 15 dB.

3.3.2. Sources of Error. Two principal sources of error act to decrease the effectiveness of the stimulated emissions radar: noise and multipath. In both the indoor and outdoor tests, narrowband interference from primary users was observed on

both the stimulation and emissions frequencies. Substantial noise also originates from the radar transmitter and couples, via the USRP board, directly into the receiver. Although the impact of these noise sources is reduced by the spread-spectrum radar signal and the post-processor, respectively, they still decrease the dynamic range of the radar. Others have shown that the noise power tends to be higher outdoors [52], and this reduced the outdoor range and noise performance. A more sensitive front-end, with automatic gain control and a higher sampling depth, could increase the radar's effective range.

Multipath can cause false targets and inaccurate distance measurements, and the effect can be severe in indoor environments. Others have conducted extensive studies of indoor multipath in real environments. Measurements conducted in an office building indicate that the multipath delay within a single room can exceed 100 ns, with a root mean square (RMS) delay spread of 50 ns [53]. Since each

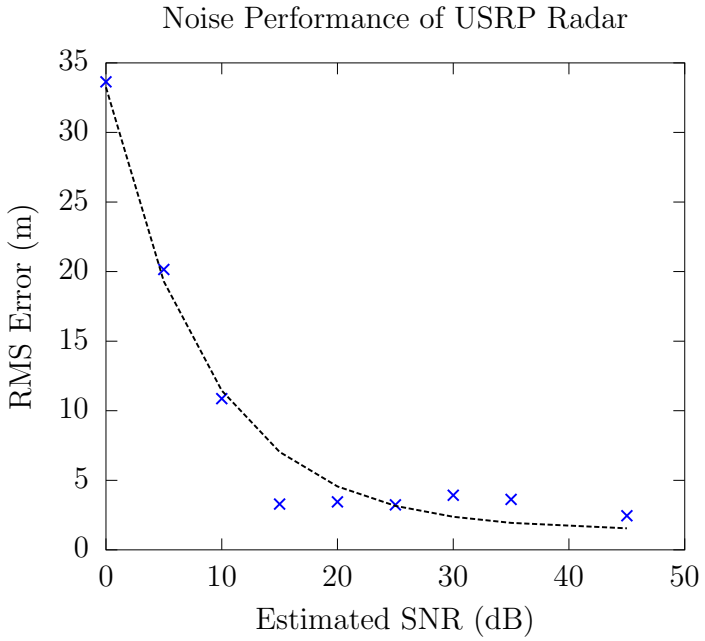

Figure 3.6: Root mean square error performance of the stimulated emissions radar. This plot includes all measurements, for both target devices, from the outdoor test. Each data point contains at least forty observations. The fit with the theoretical model (3.9) is plotted as a dashed line.

FMCW radar bin only differs by 15 ns, multipath can easily affect the results. Strong multipath negatively impacted the accuracy of the radar during the indoor tests. Techniques for reducing the effects of multipath and non-line-of-sight propagation are a crucial area of future development.

3.3.3. Device Limitations. Design differences between superheterodyne receivers make it difficult, but not impossible, to determine the absolute range. The target device imposes its own delay on the stimulated emissions as they pass through the superheterodyne front-end. This delay, while imperceptible to the user, may nonetheless differ from device to device. The GMRS receiver and the wideband receiver used in this experiment have delays which differ by 94 ns, which is approximately $3\Delta R$. This difference is too large to measure the absolute range to an unknown device, but the *relative* range estimates can still be used for two-dimensional positioning.

Time difference of arrival combines relative range estimates, taken from multiple sensors, into a two or three-dimensional position fix. Such techniques have been applied to locate devices in both line-of-sight [50] and non-line-of-sight [51] conditions. The accuracy of TDoA depends solely on the array geometry and the accuracy of each time of arrival measurement [54]. The performance measurements collected in this study could, in future work, be used to estimate the performance of a TDoA stimulated emissions locator.

3.4. CONCLUSION

The proposed wideband stimulated emissions technique can determine the range, using time-of-arrival measurements, to a superheterodyne receiver. Measurements conducted with a continuous-wave radar unit demonstrate that this technique can locate commercially-available superheterodyne receivers. The radar achieved a root mean square position error of less than five meters outdoors, and four meters

indoors, at 15 dB SNR or higher. The system is capable of functioning in non-ideal propagation environments with multipath and narrowband interference sources.

Although the system presented in this study can only measure the relative range to the device, the ability to make such measurements is crucial to the development of a true position-finding system. Extending the stimulated emissions radar to operate in two dimensions, using time difference of arrival, is a relatively straightforward task with well-characterized performance. The performance of this technique is limited chiefly by the available bandwidth. When applied to modern, high-bandwidth communications systems, stimulated emissions has the potential to enable high-precision indoor location—even when the target device does not intend to be found.

4. DETECTING AND IDENTIFYING MICROCONTROLLERS

Clocked digital systems become more and more ubiquitous with each passing year. The market for low-end microcontrollers, which can replace costly application-specific integrated circuits and discrete components, continues to grow. Many products which contain microcontrollers, including garage door openers and passive infrared sensors, can be used to initiate explosive devices [11]. The detection and identification of microcontrollers can therefore aid in the screening for and the evaluation of explosive threats.

Electronic devices can be detected using their unintended electromagnetic emissions. Any high-frequency signal, including those generated from clocks, I/O lines, and internal switching, can radiate into the environment as electromagnetic emissions. Microcontrollers can be responsible for a significant portion of a printed circuit boards' (PCB) emissions [55]. As such, they are one of the more readily-detectable components in a digital device.

Under typical operating conditions, however, microcontroller emissions are not the only signal that is present in the environment. A great number of radio-frequency (RF) emitters, both intentional and unintentional, exist in the band from 1 MHz – 600 MHz where microcontroller emissions tend to occur. A selective detector should be able to distinguish microcontroller emissions from sinusoidal signals, such as the radio receiver local oscillators in [12] and communications signals like frequency modulation (FM). In order to detect unknown devices, few assumptions can be made about the pulse shape, frequency, or jitter.

Antenna arrays offer many promising results for separating signals, but they are only part of the solution. Array processing includes spatial techniques such as beamforming [56] and blind techniques such as independent component analysis [57].

Wiener filtering can also attenuate signals from distant sources [58]. While these techniques may be useful for reducing the interference caused by high-power, intentional radio transmitters, they are less useful for identifying the type of signal being radiated. Positively identifying microcontroller emissions requires some type of classification algorithm.

Classifying devices by their unintended emissions is a well-studied topic, and many solutions exist. Others have developed techniques for identifying super-regenerative receivers [17], and previous work has shown that superheterodyne receivers can also be identified [12]. Both of these techniques use an RF stimulation signal to alter the device's unintended emissions.

Microcontrollers, however, are designed to resist ambient RF signals. Others have shown that altering the emissions of a digital device requires a prohibitively-strong electric field [59]. The stimulated detection approach from [12] cannot be applied here, but similar modeling and simulation techniques can be used to develop passive classification algorithms. An accurate model requires an understanding of where the electromagnetic emissions originate.

Microcontrollers have emissions which depend on the device's current draw. The current which flows through a microcontroller's package can form a loop, inductively driving the PCB and attached cables to radiate electromagnetic emissions [60]. In a synchronous, clock-driven processor, the vast majority of transistor switching occurs at clock edges. This results in large current spikes during each clock cycle [61]. The emissions of most microcontrollers are thus expected to be highly impulsive and dependent on the device's clock, which is typically periodic. Many different clock frequencies and resonator types are in use, however, and a generalized detection approach is required in order to detect different types of microcontrollers.

The following paper compares different methods for detecting the electromagnetic emissions of digital clock circuits. An analytic model of these clock emissions is

developed and validated using measurements of an 8051 microcontroller. This model is used, in a simulated environment, to evaluate the noise performance of several existing algorithms: the harmogram, the harmonic product spectrum, the fast folding algorithm, and linear prediction. A novel detection algorithm, the harmogrant, is proposed which uses pitch estimation with application-specific heuristics. The applicability and usefulness of each algorithm as a clock-circuit detector is considered.

4.1. METHODS

The electromagnetic emissions of microcontrollers are known to be current-dependent. If a model for the current draw at each clock cycle can be derived, it may be possible to search for the presence of microcontrollers using model-fitting techniques. Computer simulations of microcontroller current have been developed [55], but these simulations can only generate data from known model parameters. A simpler, analytic model is desirable not just for simulations, but for model-fitting as well. Several methods for modeling and predicting the emissions are presented in the following sections.

4.1.1. Autoregressive Model and Detector. An accurate, two-parameter model exists for the current draw in complementary metal oxide semiconductor (CMOS) devices. This model can be used both to simulate clock emissions and to detect them. In most digital systems, the vast majority of transistor switching occurs at the rising edge of the clock. This switching causes a substantial spike in the device's instantaneous current consumption. In [62], it was demonstrated that the current draw at the clock transition can be modeled as an exponential rise followed by an exponential decay.

The double-exponential model has two parameters: the damping ratio ξ and the natural frequency ω. These parameters can be derived from measurable RLC

properties of the device in question. As given in [62], the unit step response for the overdamped case ($\xi > 1$) is:

$$i_c(t) = \left(e^{-(\xi-\sqrt{\xi^2-1})\omega t} - e^{-(\xi+\sqrt{\xi^2-1})\omega t}\right) u(t). \tag{4.1}$$

Each clock cycle, the current draw of the CMOS system is approximated by exciting the system given in (4.1) with an impulse. This results in a periodic train of dampened pulses. An example pulse train, with typical parameters, is given in Figure 4.1. This current signal can drive unintended emissions.

Traditionally, pulse signals are detected using matched filters; this approach is common in radar systems. The performance of a matched filter has been shown to depend on the time-bandwidth product of the candidate signal [24]. The clock pulses are already very sparse in time, which limits the effectiveness of such filters.

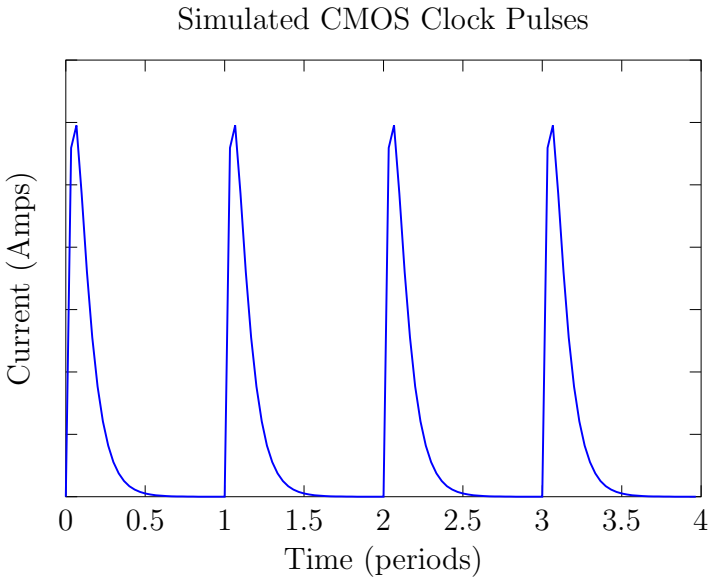

Figure 4.1: The current draw of a CMOS device. The current draw has an exponential rise and an exponential decay. The pulses shown above have $\xi = 1.093$ and $\omega = 1.22$ GHz, which were taken from a real CMOS device in [1].

More importantly, matched filters require substantial a priori knowledge of the signal's characteristics [16]. The shape of the clock emissions is not known and may vary from pulse to pulse, necessitating a large matched filter bank of candidate signals. Model-fitting techniques can offer lower computational complexity, but fitting arbitrary functions like (4.1) to received emissions is difficult. By reformulating the problem as a linear-time invariant filter, a simpler solution emerges.

Taking the Z-transform of (4.1) with a sampling period of T_s, it is shown that:

$$I_c(z) = \frac{\beta_1 z^{-1}}{1 - \frac{e^{2\alpha\sqrt{\xi^2-1}}+1}{e^{\alpha\left(\xi+\sqrt{\xi^2-1}\right)}} z^{-1} + e^{-2\alpha\xi} z^{-2}} \tag{4.2}$$

where $\alpha = T_s\omega$ and β_1 is a constant which depends on α and ξ. The filter $I_c(z)$ is an infinite impulse response filter with two feedback taps and one feed-forward tap. If given an impulse train at the clock frequency as the input, it will produce an approximation of the microcontroller's current emissions. By inspection, $I_c(z)$ only has zeros at $z = \infty$. Similar results hold for the under-damped and critically-damped cases.

The feed-forward taps only represent a single-sample delay and attenuation of the input. Since neither of these affect the overall pulse shape, and the time offset is unknown to begin with, an equivalent filter is

$$I_c(z) = \frac{1}{1 - \frac{e^{2\alpha\sqrt{\xi^2-1}}+1}{e^{\alpha\left(\xi+\sqrt{\xi^2-1}\right)}} z^{-1} + e^{-2\alpha\xi} z^{-2}}. \tag{4.3}$$

This is an all-pole filter which applies to the under-, over- and critically-damped cases, enabling it to handle emissions from devices with any damping ratio.

Although the current signal in (4.1) drives the electromagnetic emissions, the received signal may not have the same form. The voltage received by a loop probe and driving an inductively coupled antenna, for example, is proportional to the first

derivative of the current. For the over-damped case, this is not an issue, as the current signal (4.1) is composed entirely of exponentials of the form e^{Kt}, where K is a constant.

Since $\frac{\mathrm{d}}{\mathrm{d}t}\left\{e^{Kt}\right\} = Ke^{Kt}$, the derivative of $i_c'(t)$ has the same form—with the exception of some constants—as $i_c(t)$. The same holds for higher-order derivatives as well. Since the functions have the same form, the autoregressive model will have the same order regardless of which derivative the antenna receives. The autoregressive model is thus an appropriate fit for received electromagnetic emissions.

If the microcontroller emissions are assumed to be corrupted by additive white Gaussian noise, then the overall system is an autoregressive process with two taps (AR(2)). Linear prediction can be used to fit such an autoregressive model to received data. This feature makes the AR model useful as a detector.

An autoregressive process, which is depicted in Figure 4.2, can be estimated using *linear prediction*. In an AR process, an unknown excitation $\boldsymbol{e}$ is filtered with an all-pole filtesr $1/A(z)$. The filtered signal $\boldsymbol{x}$, which has been corrupted with white noise, is observed. The goal of linear prediction is to estimate the all-zero filter $A(z)$ needed to undo (i.e., inverse filter) the unknown, all-pole system filter. Linear prediction is often used in speech codecs [63].

Let $\boldsymbol{a} = A(z)$ be the system filter taps, which are a polynomial in z, and $\hat{\boldsymbol{a}}$ be the estimate of those taps. Since the all-zero filter has a finite impulse response

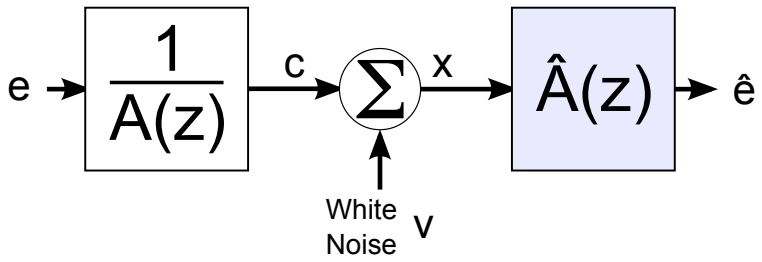

Figure 4.2: An autoregressive process. The goal of linear prediction is to estimate the taps of the all-pole filter $1/A(z)$.

(FIR), it can be evaluated with convolution. As formulated in [64] and elsewhere, the output after applying the estimated filter is

$$\hat{\boldsymbol{e}} = \boldsymbol{x} \circledast \hat{\boldsymbol{a}} \tag{4.4}$$

$$= \boldsymbol{X}\hat{\boldsymbol{a}}, \tag{4.5}$$

where $\boldsymbol{x}$ is the received signal and $\boldsymbol{X}$ is its convolution matrix.

The excitation signal of the filter, $\boldsymbol{e}$, is the portion of the signal which cannot be predicted by the linear filter. It is therefore assumed to be small. The problem then becomes one of minimizing the residuals $\hat{\boldsymbol{e}}$, which from (4.5) is equivalent to

$$\min_{\hat{\boldsymbol{a}}} ||\boldsymbol{X}\hat{\boldsymbol{a}}||_p \text{ subject to } \hat{\boldsymbol{a}}_0 = 1, \tag{4.6}$$

where $||\cdot||_p$ denotes the L_p norm. The constraint avoids estimating a filter of $\hat{\boldsymbol{a}} = 0$.

Numerically-efficient solutions, such as Yule-Walker and the Burg method, exist for the L_2 norm [64]. By measuring the power of the residual signal $\hat{\boldsymbol{e}}$, it is possible to determine how well the system fits an autoregressive model: lower power indicates a better fit. Residual power is commonly used in information theory metrics, such as Minimum Description Length, to measure goodness-of-fit [65, 66].

In order to detect microcontroller clocks, the received unintended emissions are fit to an AR(2) model using the Burg method. The power difference between the input signal and the residuals is measured as

$$\text{var}(\hat{\boldsymbol{x}}) - \text{var}(\hat{\boldsymbol{e}}) = E_{\hat{\boldsymbol{x}}}\left\{\hat{\boldsymbol{x}}^2\right\} - E^2_{\hat{\boldsymbol{x}}}\left\{\hat{\boldsymbol{x}}\right\} - \left(E_{\hat{\boldsymbol{e}}}\left\{\hat{\boldsymbol{e}}^2\right\} - E^2_{\hat{\boldsymbol{e}}}\left\{\hat{\boldsymbol{e}}\right\}\right), \tag{4.7}$$

where $E_k\{\cdot\}$ denotes the expectation function with respect to k. A detection occurs if (4.7) rises above a certain threshold. Several other algorithms are commonly used

to detect periodic signals: pitch estimation and the fast folding algorithm. These algorithms are detailed in the following sections.

4.1.2. Pitch Estimation. Since the unintended emissions are nearly periodic, they have a Fourier series representation and a time-invariant power spectral density (PSD). From Fourier theory, a periodic signal has spectral components only at multiples of its fundamental frequency f_0 [67]. This feature makes it possible to detect periodic signals by searching for harmonically-related components in the power spectrum. The PSD of a signal is typically estimated using a periodogram.

Periodograms, such as the Welch periodogram [68], estimate power spectral density by averaging successive, overlapping Fast Fourier Transforms (FFTs) together. Although higher-resolution techniques, such as multi-taper estimation, are available, the periodogram offers a reasonable (but biased) estimate at a low computational complexity [69]. The periodogram of the simulated clock emissions is given in Figure 4.3. In the frequency domain, the emissions are a series of impulses spaced f_0 Hz apart. Due to the low-pass filter effect of the pulse-shaping filter (4.3), the high-frequency components are attenuated.

Pitch-estimation algorithms, typically used in speech and music appications, are designed to detect and estimate the fundamental frequency (or "pitch") of harmonic signals such as this. Frequency-domain pitch detectors, which are studied herein, search PSD estimates for harmonically-related peaks. Time-domain algorithms, such as YIN [70] and weighted autocorrelation [71], also exist. These algorithms were designed for use in high-SNR environments, however, and may not be reliable in the presence of interfering signals.

The two pitch detectors included in this study are the harmogram and the harmonic product spectrum (HPS). Both algorithms function by aggregating harmonically-related periodogram bins together, then comparing the result with a threshold. From [72], the harmogram $H_{S^2}(f)$ of a power spectra estimate $S^2(f)$ is the sum of

power spectra

$$H_{S^2}(f_0) = \frac{1}{N}\sum_{i=1}^{N} S^2(if_0). \tag{4.8}$$

Likewise, from [73], the harmonic product spectrum $P_{S^2}(f_0)$ is the product

$$P_{S^2}(f_0) = \prod_{i=1}^{N} S^2(if_0). \tag{4.9}$$

Both algorithms accept periodograms as input, and both algorithms operate on a certain, fixed number of harmonics N. For optimal performance, N should be set to the number of harmonics present in the input signal, if known. The pitch of the signal is estimated using the maximum (local or global) of H or P. Both algorithms

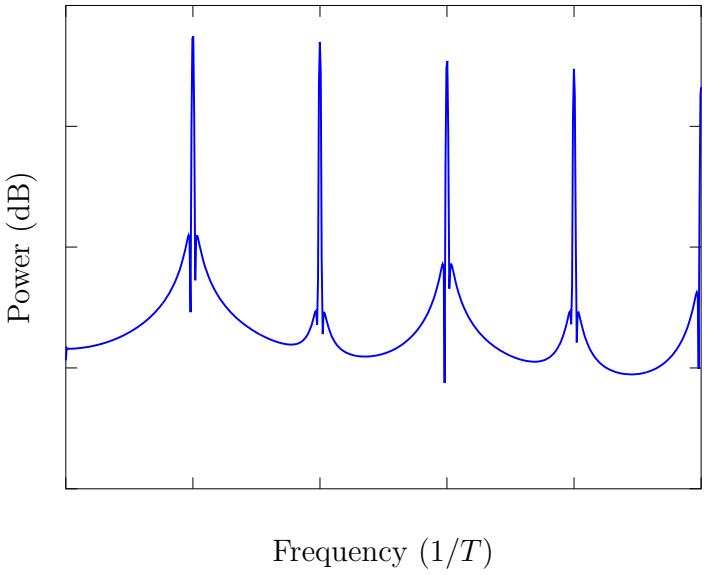

Figure 4.3: Welch periodogram of the CMOS clock pulses shown in Figure 4.1. A 4096 point window was used.. The pulse-shaping filter acts as a low-pass filter, decreasing the power of the higher-order harmonics.

are very similar: from the laws of logarithms,

$$\ln P_{S^2}(f_0) = \sum_{i=1}^{N} \ln S^2(if_0) \tag{4.10}$$

$$= N H_{\ln S^2}(f_0). \tag{4.11}$$

From (4.11), the harmonic product spectrum is essentially the harmogram of $\ln(S^2(f_0))$. The logarithm acts as a non-linear amplifier: smaller values of S^2 impact the overall sum more than larger ones.

The choice of sum or product is a selectivity/sensitivity tradeoff. HPS requires that all harmonics f_0 through f_N be large. This enables the algorithm to ignore signals that lack higher harmonics, such as pure-tone sinusoids, but it may fail to detect harmonic signals (like clock pulses) if one or more harmonics are not received. The harmogram is more tolerant of missing harmonics, but a strong sinusoidal signal can result in a false positive.

A novel pitch estimation algorithm, referred to herein as the *harmogrant*, was developed with the following heuristics in mind:

1. The fundamental frequency is the strongest harmonic.

2. At least two harmonics should be detectable.

With the above assumptions, the harmogrant G is defined as:

$$G_{S^2}(f_0) = S^2(f_0) \sum_{i=2}^{N} S^2(if_0). \tag{4.12}$$

The harmogrant requires a large, detectable fundamental frequency and a large sum of higher harmonics. It is much more tolerant of missing harmonics than HPS and should be more resistant to pure tones than the harmogram. These properties make the

harmogrant more ideal for detecting CMOS clock pulses in ambient electromagnetic noise.

4.1.3. Fast Folding Algorithm. A technique known as epoch folding can be used to estimate a single period of a periodic signal, given only noisy observations of that signal. Epoch folding is frequently used in astronomy for detecting pulsars, which have periodic emissions. This technique is of interest since, if the clock pulses are periodic and the jitter is minimal, epoch folding can estimate the actual pulse shape. Since the CMOS clock pulses have a distinctive shape, epoch folding may prove useful for detecting CMOS devices.

The epoch folding process has a simple derivation. Let $\boldsymbol{y}$ be a vector of length T which contains exactly one period of a sampled periodic signal. Let $\hat{\boldsymbol{y}}_k$ be a noisy estimate of $k \in [0, N-1]$ periods, and let the estimate be corrupted by additive, stationary random noise $\boldsymbol{\nu}_k$. Then,

$$\hat{\boldsymbol{y}}_k = \boldsymbol{y} + \boldsymbol{\nu}_k. \tag{4.13}$$

If the noise is zero-mean and the elements of $\boldsymbol{\nu}_k$ are independent of $\boldsymbol{y}$ then

$$E_k\left\{\hat{\boldsymbol{y}}_k\right\} = E_k\left\{\boldsymbol{y}\right\} + E_k\left\{\boldsymbol{\nu}_k\right\} \tag{4.14}$$

$$= \boldsymbol{y}. \tag{4.15}$$

From (4.15), an appropriate estimator of $\boldsymbol{y}$ is to fold the signal into blocks of length T and compute the mean across equivalent samples. This process is depicted in Figure 4.4 If the noise is stationary, using more sampling periods N will decrease the confidence interval of the mean.

The epoch folding process requires many addition operations, but others have shown that many of these operations are redundant. The fast folding algorithm

(FFA), developed in [74], uses a time-memory trade-off to reduce the computational complexity of epoch folding. It computes the epoch folding of M periods, at subsample resolution, between integer periods P_0 and $P_0 + 1$. The sub-sampling enables the detection of signals which have non-integer number of samples per period. The computational complexity is $\Theta(M \log_2 M)$ additions, as opposed to the $\Theta(M^2)$ additions required for the direct sum [74].

In order to test the fast folding algorithm, a reference implementation in the form of a C++ program, `ffasearch`, was obtained from [75]. The program is designed to detect impulse trains using the fast folding algorithm. Once the folds have been obtained, it is necessary to examine them for the signal of interest. Many techniques are available for doing so.

Others have developed statistical tests which enable the use of epoch folding as a detector for impulse trains. Folded signals can be tested, using Analysis of Variance, to determine if a periodicity is present [76]. A χ^2 test can also be used as a periodicity detector [77]. In [75], a constant false alarm rate (CFAR) detector is used which detects only impulse signals, which are the principle signal of interest.

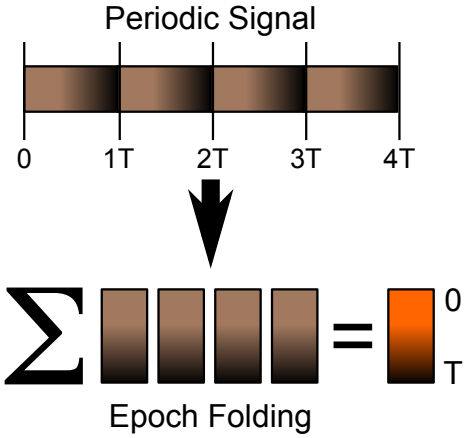

Figure 4.4: In epoch folding, a periodic signal is estimated by folding (i.e., summing) the received data from successive periods.

The CFAR detector in [75] uses cell-averaging CFAR technique to generate the test statistic d, making the detector resistant to variations in noise power from fold-to-fold. The test statistic is calculated over a fold $\boldsymbol{y}$ as

$$d(\boldsymbol{y}) = \frac{\max(\boldsymbol{y}) - \bar{\boldsymbol{y}}}{\sigma_y}, \tag{4.16}$$

where the average value of the fold, $\bar{\boldsymbol{y}}$, is calculated excluding guard bins in the vicinity of the maximum. The statistic is normalized with respect to the estimated standard deviation of the fold, σ_y. If an impulse—i.e., a large peak above the noise—is present in the fold, $d(\boldsymbol{y})$ will be large. The `ffafold` program finds folds which have large d values [75].

4.2. RESULTS

To validate the autoregressive model developed in Section 4.1.1, the unintended emissions of a real microcontroller system were measured. The measurements were compared with the AR(2) model, using epoch folding to improve SNR and information theory criterion to determine goodness of fit. After validation, the noise performance of the detection algorithms discussed in Section 4.1 were tested in a simulated environment. Although all of the tested algorithms can function as detectors, their noise performance and resistance to interference are crucial factors which impact their usefulness.

4.2.1. Model Validation. Validation testing was performed using an embedded system which included an 8051 microcontroller. The 8051 architecture was selected due to its ubiquity and relatively high-speed clock. The microcontroller under test was a Philips P89LPC932A1. The embedded system incorporates a DC power supply, mechanical push-buttons, LEDs, and a serial UART. Each of these peripherals interface with the microcontroller, which was mounted to the PCB using

a plastic leaded chip carrier (PLCC). The system board (see Figure 4.5) was assembled by hand using discrete components. This system is expected to be similar to embedded systems commonly used with explosive devices.

The microcontroller's unintended emissions were measured at close range while the device was in operation. The 8051 was configured to use its 7.377 MHz internal RC oscillator, and it was instructed to execute a test program which did nothing other than poll the I/O pins for input. A small magnetic field (H-field) probe was placed near to the 8051 in order to capture its electromagnetic emissions. The emissions were recorded using an oscilloscope.

As expected, the microcontroller has emissions which are both periodic and impulsive. The time and frequency-domain emissions, which are plotted in Figure 4.6, indicate that the emissions are related to the system clock. The fundamental

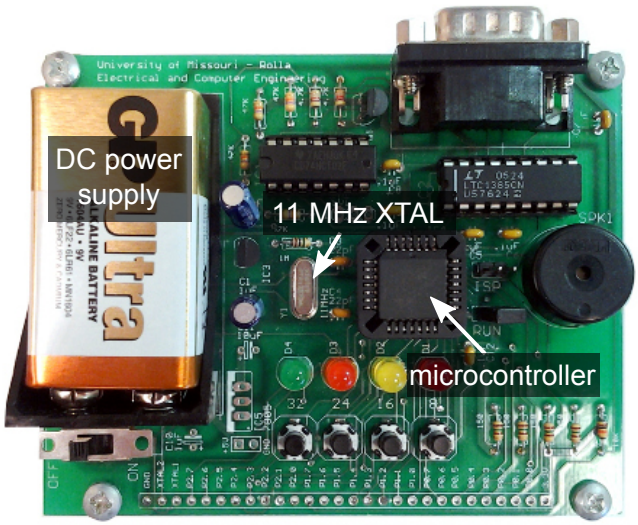

Figure 4.5: The embedded system under test. The crystal oscillator (XTAL) was not used during the preliminary measurements; the internal RC oscillator was used instead.

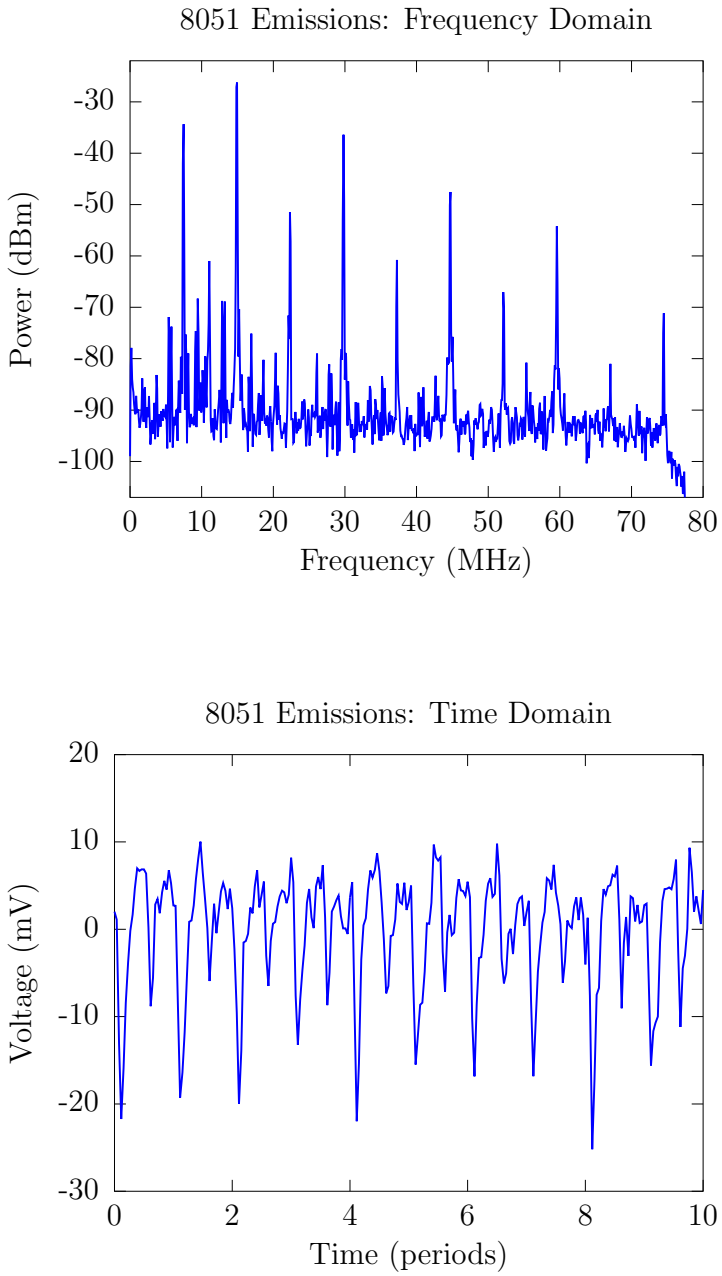

Figure 4.6: Time and frequency-domain views of an 8051 microcontroller's emissions. The clock frequency is estimated at 7.45 MHz. As anticipated, the emissions are a periodic impulse train. The pulses are in the negative direction due to the alignment of the magnetic field probe. Although the 11 MHz crystal oscillator was not used as the clock source, its harmonics are also visible in the plots above.

frequency of the emissions is approximately $f_0 = 7.45$ MHz, which is within the specified tolerance of the RC oscillator's frequency. The emissions are a harmonic signal, and the first ten harmonics (f_0 through f_9) are present.

Epoch folding was used to obtain an estimate of the pulse shape. Although the fast folding algorithm can detect the presence of microcontroller emissions, it is less useful for estimating the period: the FFA's output typically contains spurious peaks in the vicinity of the true period. Since the goal is to make a very fine estimate of the pulse shape, the period was estimated directly in the frequency domain, and ordinary epoch folding was performed.

A multi-taper power spectral density (MTPSD) estimate was used to estimate the period of the emissions. The MTPSD is an unbiased spectral density estimator, and it has favorable resolution properties for making very fine frequency estimates [69]. To limit the effects of long-term oscillator drift, the epoch fold contained only 769 clock periods of data. The emissions were then resampled, using a polyphase filter bank, to exactly 26 samples per period.

The re-sampled emissions were folded across two separate periods ($2T$ samples). The results of the fold, which are plotted with error bars in Figure 4.7, indicate that the double-exponential AR model is a suitable approximation for clock emissions. The variance of the folding bins is less than 7% of their magnitudes, which indicates a good fit for the periodic signal model. The smaller peaks visible in the figure occur at the falling edge of the clock, where another substantial current draw occurs due to switching within the clock tree.

In Figure 4.8, the same data is folded across a single period. Linear prediction is used to fit an AR(2) model to the data, and a single clock pulse is generated using the estimated system filter. Both signals are aligned in time and normalized to a peak value of one. The result of this process indicates that the AR(2) model is a

good fit in the vicinity of the main peak but loses accuracy elsewhere. This loss of accuracy is due to a secondary peak, visible at approximately $0.6T$.

This secondary peak, which is located half a period away from the main peak, is caused by additional transistor switching. This additional switching takes place at the falling edge of the clock, whereupon the clock tree resets itself for the next cycle. The presence of this second peak will not affect the harmonic techniques, as the signal is still periodic with a period of T. It may, however, reduce the effectiveness of linear prediction with real CMOS emissions.

Although the emissions appear visually to be a good fit for the AR(2) model, goodness-of-fit can be determined mathematically. If the signal is more complex than the AR(2) model presumes, a higher autoregressive model order would provide a better representation—i.e., a lower residual power. The optimum autoregressive

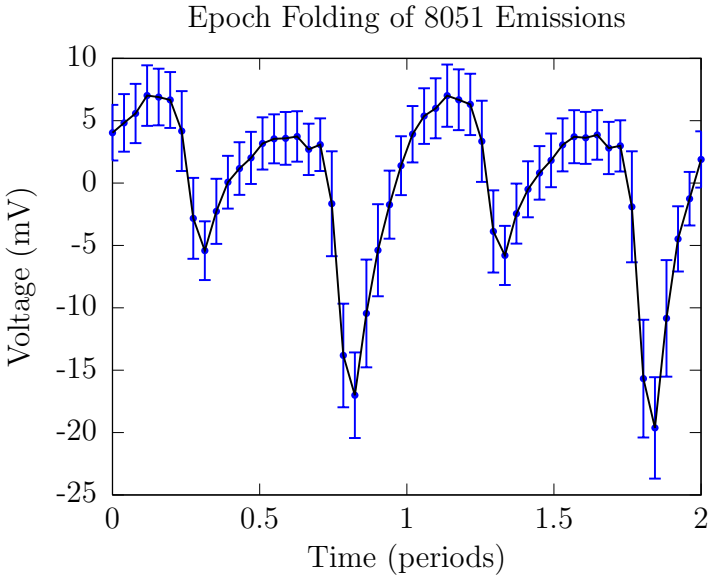

Figure 4.7: Epoch folding of 8051 electromagnetic emissions. The folding includes two separate clock periods and is plotted with standard deviation error bars.

model length can be found using information theory criterion, such as the Minimum Description Length (MDL).

As formulated in [65], the MDL finds the minimum model order that is required to represent a signal. It is evaluated as:

$$\mathrm{MDL}(i) = L \log \mathrm{var}(\hat{\boldsymbol{e}}) + i \log L, \tag{4.17}$$

where i is the linear prediction order and L is the length of the input vector $\boldsymbol{x}$ from (4.5). The epoch-folded emissions from the 8051 system were tested using linear predictors of various orders, $i = 1$ through $i = 10$.

The results of this computation, given in Figure 4.9, indicate that the MDL reaches a local minimum value at $i = 2$. The global minimum occurs at $i = 4$, but

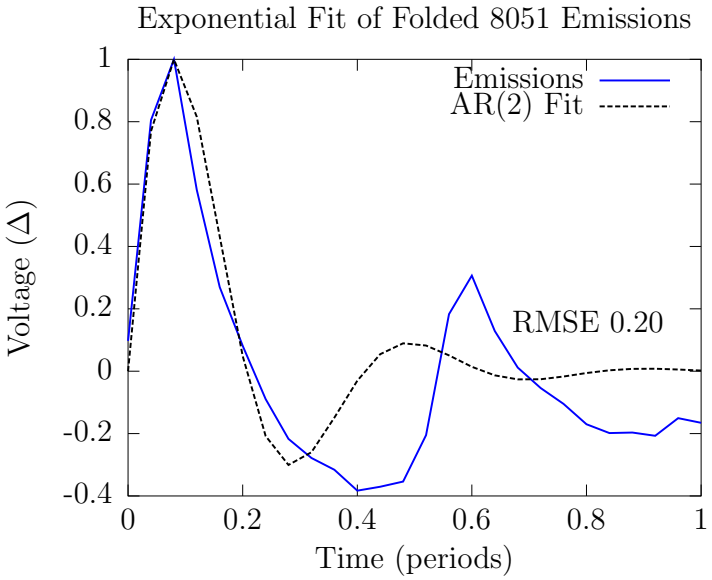

Figure 4.8: The epoch-folded 8051 emissions and the ideal CMOS pulse determined by linear prediction. The epoch folding is plotted with a solid line, and the ideal CMOS pulse is plotted with a dashed line. The second peak near $0.6T$ occurs at the falling edge of the clock, where another substantial current draw takes place.

the difference is not particularly significant. The AR(2) model is a good choice to represent this data set.

4.2.2. Simulated Environment. Since the autoregressive model fits real CMOS emissions, detection algorithms can be tested through simulation. As in Section 2.3, a simulated environment allows for controlled conditions, such as signal-to-noise ratio, which are difficult to replicate consistently in a real system. The CMOS clock pulses from Figure 4.1 were used as a test signal. The simulator assumes that the channel corrupts the signal with additive white Gaussian noise.

White Gaussian noise is often a poor approximation of a radio channel. Channels may exhibit Rayleigh fading [78], frequency-selective fading [79], multipath propagation [53], correlated noise, or numerous sources of man-made interference. The goal of these tests is not to simulate radio propagation, however, but to determine the relative performance of the detectors. Remedies for non-ideal noise conditions exist, and some of them are detailed in Section 4.3.1.

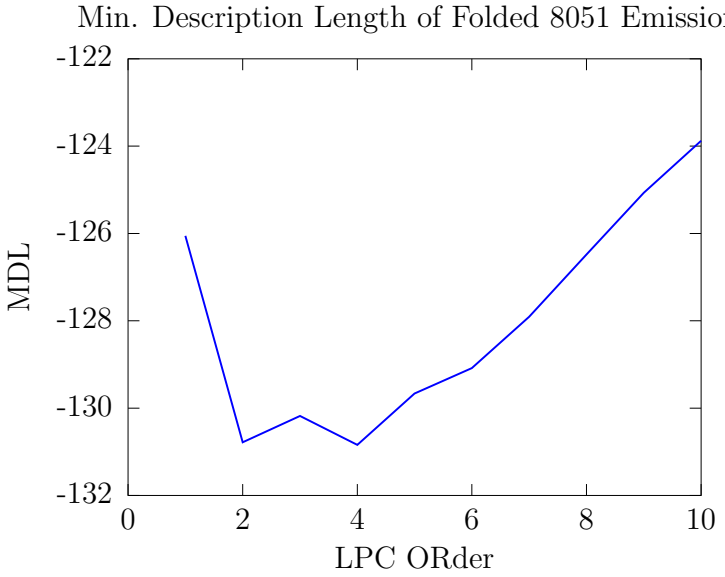

Figure 4.9: The minimum description length (MDL) statistic. The MDL indicates that the AR(2) model is an appropriate approximation of 8051 clock emissions.

The simulator generates two test vectors,

$$\boldsymbol{x} = \boldsymbol{c} + \boldsymbol{\nu} \tag{4.18}$$

$$\boldsymbol{n} = \boldsymbol{\nu}, \tag{4.19}$$

where $\boldsymbol{c}$ is the CMOS emissions and $\boldsymbol{\nu}$ is white, zero mean Gaussian noise (see Figure 4.2). The power of the noise is used to control the signal-to-noise ratio. The vectors $\boldsymbol{x}$ and $\boldsymbol{n}$ are normalized to unit variance and used, individually, to test the algorithms. The test statistics from the linear prediction (4.7), harmogram (4.8), HPS (4.9), harmogrant (4.12), and FFA (4.16) algorithms are evaluated on each of these inputs, producing output vectors of true positives and true negatives.

These test statistic vectors are used to generate Receiver Operating Characteristic (ROC) curves for each algorithm. The ROC curves are generated as in Section 2.3.2. A threshold detector, with the threshold set to various values, classifies each of the above test statistics as a "detection" or a "non-detection," and the true positive rates and false positive rates are determined through simulation. In cases where the test statistic contains multiple values—i.e., the harmogram power at various frequencies—only the maximum value is considered.

The area under the ROC curve (AUC) is a commonly-accepted measure of performance. The area represents the probability that a randomly-chosen true positive will have a larger-valued test statistic than a randomly-chosen true negative [80]. If the AUC is 1.0, the test perfectly separates true and false positives with a definite decision threshold in between. If the AUC is 0.5, the test yields no useful information as a detector.

The algorithms included in this study are not just detectors—they have inherent estimation capability as well. Both linear prediction and FFA can estimate the pulse shape, and the FFA and pitch estimators can estimate the fundamental

frequency. For the purposes of this test, the estimation capability is not tested: only the algorithms' performance as a detector is considered.

In addition to white Gaussian noise, sinusoidal interference is considered. Sinusoidal signals can occur as communications signals (or as components thereof) or as unintended emissions from radio receivers [12]. Since sinusoidal signals are strongly concentrated in the frequency domain, they are among the most likely signals to cause false positives with the pitch estimation algorithms. They may also disrupt the linear prediction algorithms, as sinusoids also have an autoregressive representation [64].

Two test cases, with a single interfering sinusoid, were considered. The period of the sinusoid was $0.75T$, placing it halfway between two harmonics. The power of the sinusoid was fixed at +10 dB above the noise power for the first test. For the second test, it was defined to be +10 dB above the signal power instead, making it a stronger signal. The interfering sinusoid is part of the noise vector $\boldsymbol{n}$, making it present regardless of whether or not the signal includes CMOS emissions. The results of this simulation procedure are discussed in the following section.

4.2.3. Simulation Results. The simulation program was executed using the CMOS emissions given in Figure 4.1 as input. SNRs between -15 dB and -35 dB were tested, with one hundred independently-generated noise vectors $\boldsymbol{\nu}$ tested at each SNR level. Thirty thousand periods, with thirty samples per period, were simulated.

The pitch estimation algorithms and the FFA were limited to search the same range of periods: from $0.7T$ to $3.33T$. This limitation was put in place to reduce the noise found in FFA folds of low-frequency data. The pitch detection algorithms used a minimum of $N = 4$ harmonics and a maximum of $N = 5$ harmonics. After simulating, the area under the curve (AUC) was calculated for each test case. The results are summarized below.

For white Gaussian noise, plotted in Figure 4.10, the harmogrant outperformed all other algorithms under each tested SNR. The results were similar to the traditional

harmogram, however, and the additional selectivity from the multiplication operation provides only modest improvements. Linear prediction was less effective, and did not perform substantially better than any of the pitch estimators. All the techniques perfectly separated true and false positives above an SNR of -15 dB. In this test case, the harmogrant offers a 4 dB increase in noise performance over the fast folding algorithm.

The strong and weak sinusoidal results are plotted in Figure 4.11. The weak sinusoidal stimulation had only a minimal effect on the algorithms. Even the harmogram, which has no inherent resistance to pure tones, was able to suppress the unwanted signal. The strong sinusoid, whose results are plotted in Figure 4.11, causes problems, however.

The unmodified harmogram selected, without fail, the strong interfering sinusoid as the most significant (i.e., strongest) signal of interest. Due to normalization,

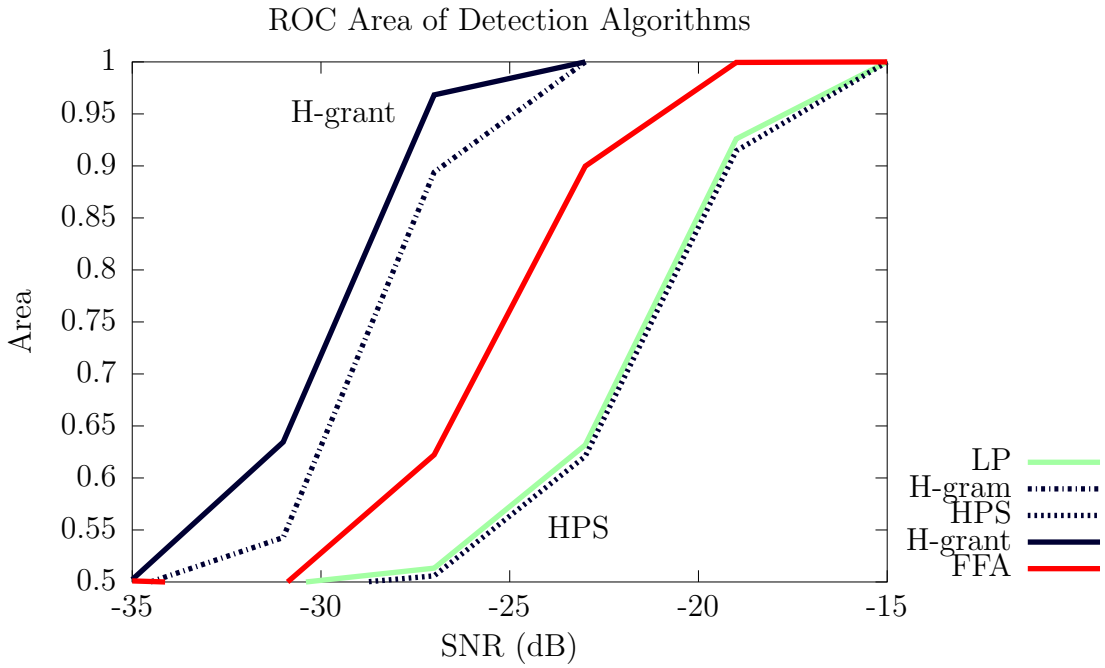

Figure 4.10: Simulation results for CMOS signal in white noise. The harmogrant ("H-grant") offers superior performance in all test cases.

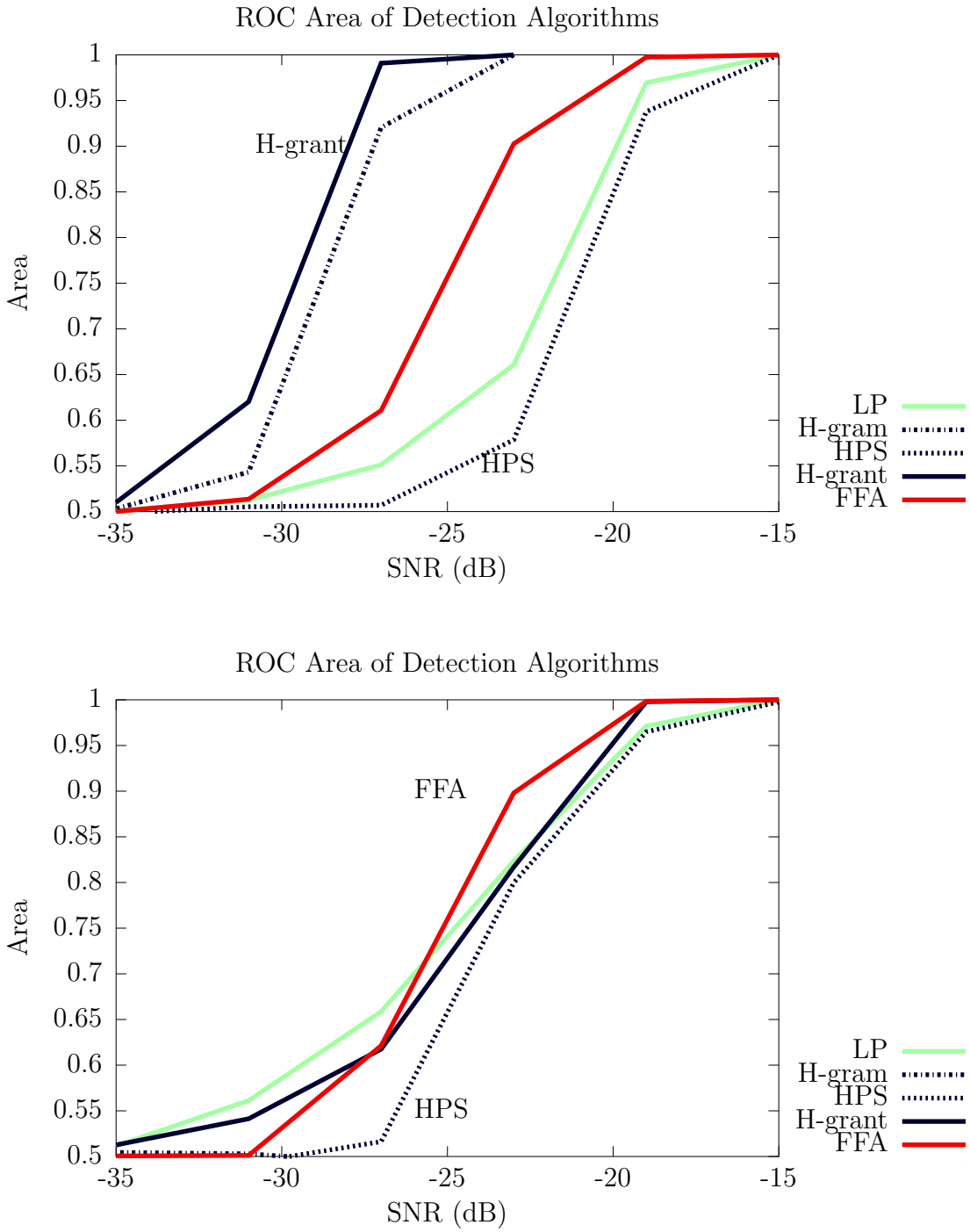

Figure 4.11: Simulation results for the weak sinusoid and strong sinusoid. The weak sinusoid (top) had minimal impact on the results, while the strong sinusoid (bottom) substantially reduced the noise performance of most algorithms. The Fast Folding Algorithm is essentially immune to interfering sinusoids.

the periodogram-estimated power of the interfering sinusoid was slightly lower in the "signal + noise" case than it was in the noise-only case. This reversed the behavior of the detector statistics, resulting in AUCs that were below 0.5. The harmogrant's performance was also degraded by the interference—though only slightly.

The linear prediction algorithm performed well in the strong sinusoidal interference case—slightly better than it did for pure additive noise. Although the sinusoidal signal is autoregressive, it has poles near the unit circle, and the pulse signal results in much lower-energy residuals. Since linear prediction minimizes the residuals, it converged preferentially to the CMOS pulses.

The FFA and HPS were, predictably, unaffected by sinusoidal interference of any variety. The FFA's detector is highly specific to impulses, and HPS imposes a large penalty for missing harmonics, giving them almost complete immunity to these narrowband interferers.

4.3. DISCUSSION

The pitch estimation results clearly demonstrate the trade-off between sensitivity and selectivity. The harmonic product spectrum is too selective to have good noise performance. Due to the low-pass fall-off of the CMOS clock pulses, noise tends to make the higher-order harmonics undetectable, rendering HPS inoperative. The harmogram offers better noise performance, but it is quite vulnerable to single-tone sinusoids. The harmogrant, a combination of the two algorithms, performs better in all of above test cases.

The time-domain algorithms—linear prediction and epoch folding—have poor noise performance. Problems with the detector statistic limited the performance of the FFA. Despite normalizing by the estimated noise in (4.16), the statistic exhibits frequency-dependent behavior. Epoch folds of white noise have a much higher power

level near DC than they do in the higher frequencies. Further study may yield a more robust noise estimator. Although the time-domain algorithms have poorer noise-performance, they may be more effective at discarding spurious, high-power signals in the high-SNR regime.

Although these results are promising, the simulated environment cannot accurately model all of the behaviors of a CMOS device. Devices such as microcontrollers may execute a different instruction each clock cycle, causing the magnitude—or perhaps even the duration—of the current pulses to vary. The impact of antennas, and the potential availability of near and far-field radiation, is also an important consideration. These behaviors are best tested by measuring real CMOS devices in an actual RF propagation environment.

A number of issues remain before these algorithms can be implemented in a practical digital device detector, however. Two of these issues—noise estimation and clock jitter—are addressed in the following sections.

4.3.1. Constant False Alarm Rate. An optimum Neyman-Pearson detector uses a threshold test to determine if a signal of interest is present. The value of the threshold depends on the desired probability of false alarm, which is set by the user. Correctly setting this threshold requires knowledge of the probability density function (pdf) of the noise [81], but this pdf is rarely known in practice. In order to have a fixed probability of false alarm, it is necessary to set the threshold from the *data* itself.

This family of techniques is known as Constant False Alarm Rate (CFAR). In a CFAR algorithm, the noise level is first estimated from the data. Bins which exceed a certain threshold, compared to the noise level, will trigger a detection. Sometimes this threshold is set assuming that the noise has a particular distribution [82,83], but other approaches simply use a constant gain above the noise level. CFAR can be applied to, and is frequently applied to, power spectral density estimators.

In periodograms, CFAR can estimate the noise level for each bin individually. This makes the periodogram more robust against frequency-selective fading. Such fading can occur as the result of, for example, non-flat frequency response in the receiver or multipath propagation. While equalization can remove most of these channel effects, most equalizers depend on knowing the transmitted signal very precisely—which is difficult in this application [84].

CFAR processors operate on the assumption that any frequency-selective effects are gradual—i.e., the channel's gain varies slowly with respect to frequency. This enables the detector to assume that bins which are nearby in frequency have similar noise powers. For each bin, the noise level is estimated using the surrounding bins. If the bin under test contains a signal, that signal may also leak or spread into surrounding bins. Hence, the closest bins are excluded from the noise estimate. The process is illustrated in Figure 4.12.

A number of different noise estimation techniques exist. Cell-averaging CFAR (CA-CFAR) estimates noise using the mean average, while order-statistic CFAR (OS-CFAR) uses an order statistic. Each method has its own set of advantages and drawbacks, but OS-CFAR has been shown to outperform CA-CFAR in most cases [85]. Regardless of the technique in use, a CFAR processor is indispensable for a practical CMOS clock detector.

4.3.2. Jitter. Microcontroller oscillators can exhibit considerable drift, and any period estimate may not be valid for long. Systems which do not have particularly demanding real-time constraints can use low-cost RC oscillators, and these oscillators may have substantial long and short-term drift. Even crystal oscillators, which offer higher precision, are not immune to environmental conditions [86].

Some oscillators deliberately add jitter in order to reduce their apparent unintended emissions. These oscillators, which are known as spread spectrum clock generators (SSCGs), are of particular interest since they add jitter deterministically—and

are thus simpler to model than random drift. They are also of interest because they may be more difficult to detect than standard oscillators—with pitch estimators in particular. It is worth noting that an SSCG does not actually reduce the radiated power—it merely spreads the radiated power over a wider range of frequencies.

SSCGs add jitter by making the oscillator's target frequency a function of some other periodic function. Each period, the time until the next clock pulse is selected using the output of this spreading function. The spreading function is typically symmetric about the oscillator's "true" period, making the oscillator an accurate timekeeper, on average. Triangle waves are popular spreading functions and are used in practical SSCG devices [87, 88].

In order to simulate the effect of a jittery oscillator, a spread spectrum clock generator was used in the simulation. The simulated SSCG used a triangle-wave

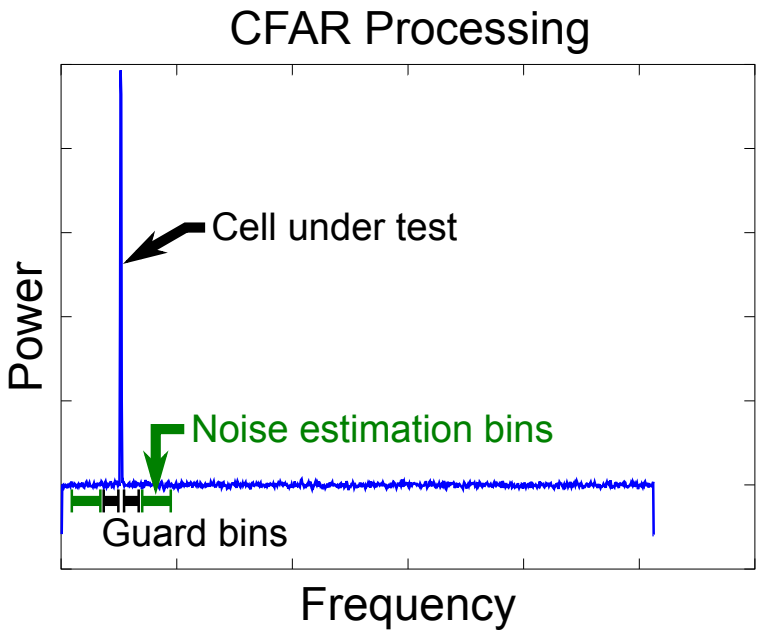

Figure 4.12: The CFAR algorithm estimates the noise level for each bin using the surrounding bins. The bins closest to the bin under test are ignored (guard bins). This process is repeated for each and every periodogram bin. The bins used for estimation are sometimes referred to as training bins.

spreading function that was 263 clock periods long and resulted in a maximum deviation of ±1% of the oscillator's true period. These values were taken from a real SSCG documented in [87].

The simulation results, which are plotted in Figure 4.13, show the fast folding algorithm is particularly sensitive to jitter. The sub-sample folding accuracy of FFA is more harmful than helpful in this case, as the peaks from the clock pulses are spread into many different bins. The pitch estimators, which use only 2049 bins to represent the entire signal, are much less sensitive to jitter. A decimation process may make the FFA more resistant to jitter, but the pitch estimators offer better performance at lower computational complexity.

In future work, cyclostationarity analysis may yield a more sensitive detector for SSCGs. Unlike a stationary process, which has time-invariant statistical properties, a cyclostationary process has statistical properties which vary cyclically (i.e.,

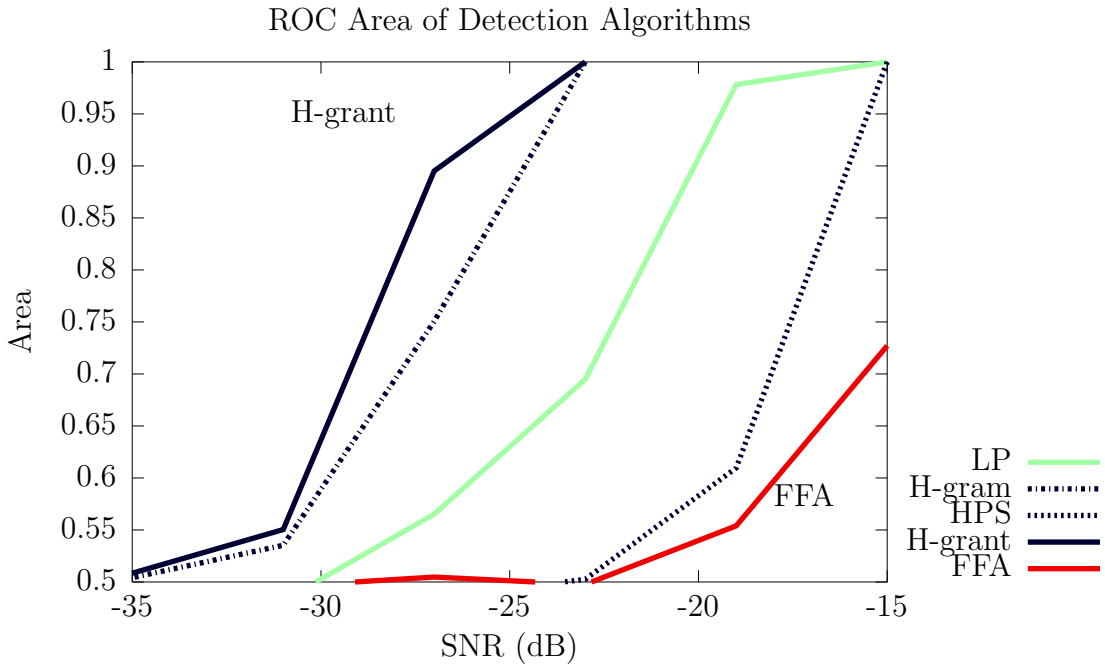

Figure 4.13: Simulation results for a jittery CMOS signal. The Fast Folding Algorithm is particularly sensitive to jitter.

periodically) in time [89]. In this case, the power spectrum of SSCGs varies cyclically with respect to the spreading function. Cyclostationarity analysis has been proven to be effective at detecting chirp radar [90], and it may be useful for detecting these triangle wave-spread pulse trains as well.

4.4. CONCLUSION

Simulations indicate that pitch estimation algorithms offer the best noise performance for detecting digital devices. These algorithms operate in the frequency domain using periodograms as input, which makes them simple to implement on any real-time device which has an FFT library. Periodograms have behaviors and trade-offs, such as time/frequency resolution and windowing, which are well-understood [23, 47, 91]. The harmogram, harmogrant, and the harmonic product spectrum do not substantially increase the computational complexity of the periodogram, which is given in [68].

While all of the pitch estimation algorithms performed well, the harmogrant provided the best sensitivity and selectivity for this application. The harmogrant, which is a minor, heuristic modification to the harmogram, has proven to be robust against sinusoidal interference, low SNR, and typical jitter. This pitch estimation technique offers a 4 dB gain in noise performance over the fast folding algorithm. These findings re-enforce the usefulness of the Welch periodogram, and its relatives, for detecting periodic signals.

Although the pitch estimation methods offer the highest performance, the time-domain techniques are also useful. With sufficient signal-to-noise ratio, linear prediction and the fast-folding algorithm also function "perfectly" with a ROC area of 1.0. The fast folding algorithm is the most selective technique available: it only

detects impulse train signals. This selectivity may prove essential in real-world scenarios, where unexpected interference signals are present. Additional refinements may make the FFA more robust against noise and jitter.

Linear prediction offers no particular advantage over the other techniques, but the autoregressive model it is based on is useful for modeling clock emissions. Comparisons with real data, gathered from an 8051 microcontroller, indicate that a second-order autoregressive model is a reasonable approximation of clock emissions. The model holds even when the emissions are received via a loop probe, which uses inductive coupling.

These findings, while preliminary, demonstrate the feasibility of building a digital device detector. The harmogrant and fast folding algorithms have promising simulated results and, in future work, could be tested in a real-time detector under real propagation conditions. With additional measurements and testing, the methods proposed herein could enable the rapid discovery of digital devices.

APPENDIX

Measuring stimulated emissions requires two vital radio frequency (RF) components: a transmitter and a receiver. In prior research conducted in Seguin [92], these measurements were conducted using traditional lab equipment: signal generators, spectrum analyzers, and oscilloscopes. This approach has a number of important drawbacks, however. Most signal generators are strictly-analog systems which can only perform analog modulations, such as AM and FM. This necessitates the use of additional hardware, such as waveform generators, to produce the desired stimulation signal.

The receiver side, depending on the exact configuration, was similarly complicated. A variety of analog mixers and filters were used to lower the frequency of the unintended emissions, allowing them to be sampled at lower rates. Digital sampling was performed using oscilloscopes, which posed their own set of difficulties. Oscilloscopes have a finite memory space for digital samples, and the oscilloscopes used in [92] could only capture several consecutive milliseconds of data before exhausting this space.

Once the samples were obtained, they were transferred to a personal computer (PC) for further processing. This step required the use of slow, low-throughput IEEE-488 (GPIB) interfaces. As a result, the stimulated emissions system developed in [92] could only sample intermittently, and the data transfer itself introduced over one second of latency. The complete measurement setup consisted of numerous pieces of bulky, fragile equipment, and it was not particularly portable. This system was built as part of the preliminary investigation of the stimulated emissions approach, which was successful, however more convenient solutions exist.

Software-defined radio (SDR) platforms replace purpose-built analog communications circuitry with high-speed digital signal processing (DSP). As its name implies, most of the radio signal processing takes place in software: typically on a standard PC. An SDR digitizes radio signals in much the same way that a sound card digitizes audio, except that the process takes place at a much higher speed. The components of an SDR system are illustrated in Figure 5.1

The hardware component of an SDR system, often referred to as the "front-end," is designed to be minimalist and flexible. An analog radio receiver—either superheterodyne or direct-conversion—is used to select the desired frequency and bandwidth. The signal is then sampled using high-speed analog to digital converters (ADCs). A comprehensive overview of the digitization process can be found in [93]. Some ADCs operate fast enough that the analog front-end can be omitted entirely.

The limiting factor in an SDR system is, typically, the interconnect between the front-end and the host computer. This interconnect, such as Universal Serial Bus (USB) or PCI Express, has limited throughput—i.e., USB 2.0 has a maximum transfer

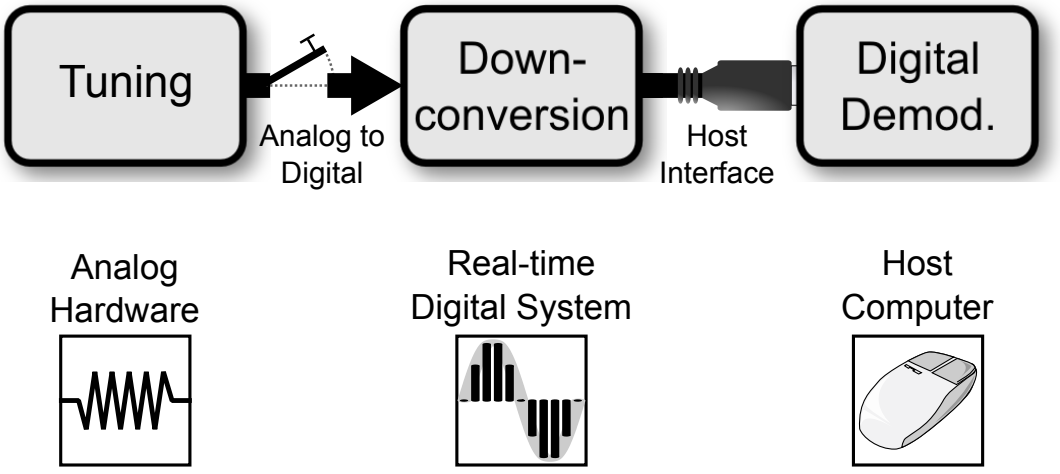

Figure 5.1: A software-defined radio system. The hardware components, including the real-time digital system, are designed to be as minimalist as possible. This grants the host computer more flexible access to the radio signal and spectrum.

rate of about 32 MiB/s. In order to meet real-time deadlines, it is necessary to limit the data rate to that of the interconnect. This is accomplished by discarding the unnecessary portions of the radio signal: a process known as digital down-conversion.

Digital down-conversion is the digital equivalent of analog frequency translation. The signal is shifted in frequency until the band of interest is centered at baseband. (Quadrature sampling is used to preserve the magnitude and phase of the signal.) The signal is then band-limited, using digital filters, to the frequency range of interest. Once it has been filtered, the sampling rate can be reduced without distorting the signal. The reduction in sampling rate greatly decreases the amount of data that must be transferred and processed.

Once the data is transferred to the host computer, application-specific signal processing is performed. Typically, these tasks include demodulation and, for data signals, framing. In stimulated emissions, the goal is to search the down-converted radio signal for the presence of some known stimulation signal. The algorithms to do so can be written in ordinary, general-purpose computer languages such as C++ and Python.

The principal advantage of software-defined radio is flexibility. The same SDR platform can perform many different tasks, often simultaneously. Changing the DSP algorithm is as simple as altering the software. Computer systems have access to advanced user interfaces, built-in debuggers, and nearly-unlimited storage, making them an attractive alternative to dedicated hardware. It is no surprise that SDRs are popular with research and other non-recurring engineering tasks [94].

The papers in Section 2 and Section 3 developed two major software-defined radio projects, both for research and for demonstration purposes. These projects, which are detailed in the next two sections, are intended to validate the effectiveness of stimulated emissions. They also, by extension, demonstrate the usefulness of SDR to research and academia.

MATCHED FILTER DETECTOR

Many different SDR platforms are available, ranging from hobbyist kits ($20 U.S. Dollars) to purpose-built computer systems for maximum sensitivity and throughput ($7000 U.S. Dollars or more). The matched filter detector used in Section 2 was built using the Ettus Research Universal Software Radio Peripheral (USRP), which was selected due to its proven performance and wide range of available transceiver modules. The USRP's companion software, GNU Radio, is designed to support real-time designs. The DSP operations (i.e., functions) are described using the Python scripting language. When the system is started, these operations are executed continuously on the incoming data from the SDR [21].

The matched filter detector is designed to detect superheterodyne receivers using the method outlined earlier in this chapter. As per Figure 2.7, the system detects radio receivers by transmitting a 5kHz linear FM chirp and searching for the chirp on another, defined frequency using a matched filter. When the program is started, it generates a baseband, complex-sampled chirp of a user-specified length. The chirp's matched filter, which is a finite impulse response (FIR) digital filter, is then derived and stored. This detector is implemented entirely using the USRP's companion software, GNU Radio.

The program then instructs the USRP to transmit this chirp repetitively and sample the radio spectrum at the up-mixing emissions frequency. The received signal is then filtered through the matched filter. If a radio receiver is present, the matched filter will output an impulse-like spike every chirp period. A threshold detector is used to decide if a radio receiver has been detected: The power output of the matched filter is compared with a fixed, user-specified threshold, and a detection is declared if the power exceeds the threshold [81].

The matched filter detector includes a simple GUI, shown in Figure 5.2, for setting and viewing the detector's threshold. A visual and audible alarm are activated if a radio receiver is detected. The detector operates in real-time, updating its display continuously as new data is received. The complete hardware setup, as shown in Figure 5.3, fits neatly on a tabletop and is easy to transport.

This real-time implementation offers substantial advantages over the sample-then-process design used for initial investigations in Seguin. Long-duration chirps,

Figure 5.2: The simple GUI for the matched filter detector. The image of the radio receiver indicates that a device has been detected.

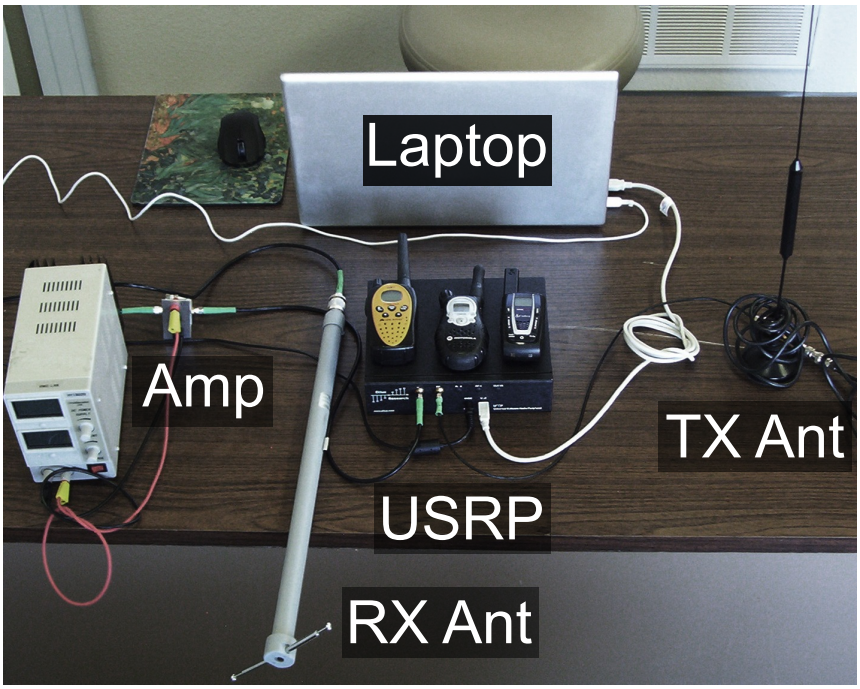

Figure 5.3: The assembled USRP test setup fits neatly on a table top. It can be disassembled and stored in a small box for transport.

which exceed one second in length, can be used without difficulty. Troubleshooting physical problems, such as antenna leakage or cross-coupling, is vastly simplified when the detector statistic updates quickly. The matched filter detector program offers an easy-to-understand demonstration of the stimulated emissions technique. Although the hardware used in [92] was commonly available, and more than adequate for a preliminary study, the SDR platform resulted in a much simpler, easy-to-use system.

SOFTWARE-DEFINED RADAR

Locating superheterodyne receivers using the time-of-arrival method, as discussed in Section 3, requires high-precision timing. The SDR must be capable of accurately measuring the time difference between the transmission of the stimulation and the reception of the emissions. For speed-of-light signals, a timing error of just ten nanoseconds translates into one meter of range error. This is a strict real-time synchronization demand which cannot be met using general-purpose computer programs. Designing an SDR to meet these demands is a challenging task.

From [12], it is known that superheterodyne receivers are highly responsive to linear FM chirps. Using a technique known as frequency-modulated continuous wave (FMCW) radar, it is possible to use similar chirp signals for ranging in addition to detection. In continuous-wave radar, the power of the transmitted stimulation is kept constant. Constant-power signals perform well with systems that use solid-state, low-noise amplifiers—as superheterodyne receivers typically do [40]. FMCW has a computationally-efficient implementation which makes it ideal for SDR.

In [95], it is demonstrated that delaying a linear FM chirp in time is equivalent to shifting it in frequency. In radar systems, the time-delayed return signal—in this case, the emissions from the target device—appears to be slightly shifted in frequency. This frequency shift, as shown in Figure 5.4, can be estimated by finding

the instantaneous difference in frequency between the transmitted stimulation and the received emissions. This difference can be found using mixers.

In the mixer implementation, the received emissions are mixed with a time-reversed version of the transmitted stimulation. The result is a low-frequency "beat" signal which contains the range information. Traditional estimators of frequency, such as the Fast Fourier Transform (FFT), can be used to estimate the beat signal's frequency—and thus the range. This design is ideal for use on software-defined radio platforms: The mixing is a mathematically simple—but time-sensitive—operation, whereas the frequency estimation can benefit from the processing power of a general-purpose computer.

To fulfill the real-time requirement, an FMCW front-end was added to the USRP. The front-end generates the linear FM chirps and performs a simultaneous de-chirp of the received emissions. To guarantee a fixed delay, these operations were

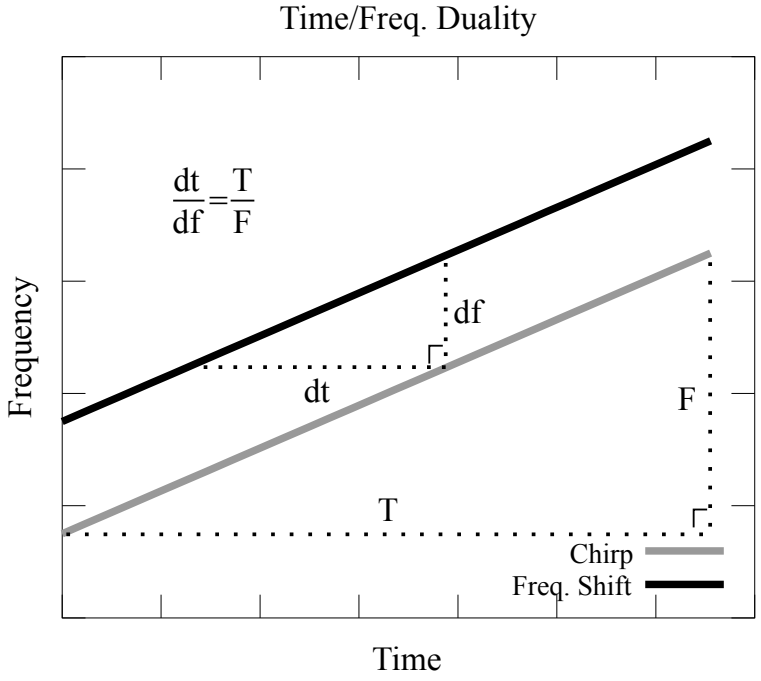

Figure 5.4: Delaying a linear FM chirp in time by some amount dt is equivalent to shifting it in frequency by some amount df. This relationship is easy to visualize from the proportional triangles given above. By estimating the frequency difference df, it is possible to estimate the time delay dt.

implemented in the USRP's field-programmable gate array (FPGA). The FPGA typically performs the high-speed digital down-conversion (see Figure 5.1), but it supports loading user-customized instruction sets as well. This customization is made possible, in part, by the USRP's open-source design. After de-chirping, the resulting beat signal is down-converted and sent to the host computer.

The host computer then estimates the frequency of the beat signal. A two-dimensional FFT, as per [43], simultaneously estimates both the range to and Doppler shift of a target. The entire software-defined radar system is depicted in Figure 5.5. Since it was designed for stimulated emissions, this radar system has one additional feature: it can transmit and receive on different, arbitrary frequencies. This enables the radar system to receive and detect up-mixing emissions from superheterodyne receivers.

This prototype system demonstrates the extensibility of software-defined radio platforms. Owing to their advanced computer software and re-programmable circuitry (i.e., FPGAs), such platforms can be modified to function far beyond their

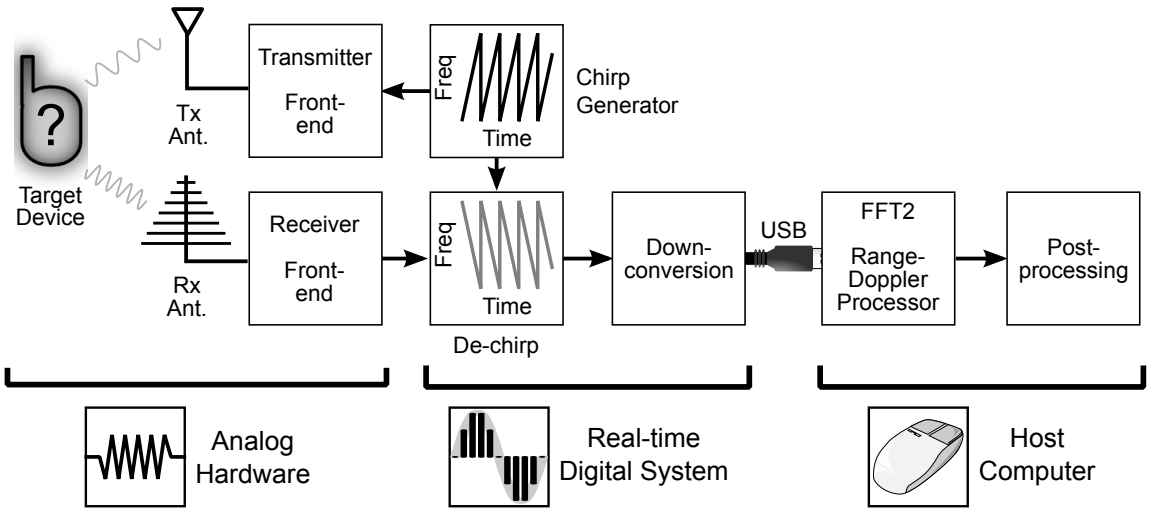

Figure 5.5: Block diagram of the software-defined radar. A chirp generator, and a synchronized de-chirp function, were added to the USRP's FPGA firmware. The range-doppler processing is carried out on the host PC. Adapted from [13], © 2013, IEEE. Used with permission.

original design specifications. The system described above was successfully tested in [13], where it accurately measured the range to various superheterodyne receivers. While isolation problems between the transmitter and receiver substantially reduced the system's performance, these problems occurred in the analog front-end and are not specific to SDR.

As this research demonstrates, software-defined radio products greatly increase the accessibility of the radio spectrum to academic researchers. These devices can facilitate the development of novel communications and signal processing techniques, and it is worthwhile to consider them whenever rapid prototyping is desired.

BIBLIOGRAPHY

[1] Y. Fu, G. Burbui, and T. Hubing, "An improved model for representing current waveforms in CMOS circuits," Clemson University Vehicular Electronics Laboratory, Tech. Rep. CVEL-06-001, Oct 2006.

[2] 110$^{\text{th}}$ United States Congress, "Department of homeland security appropriations bill, 2009," GPO, Washington D.C., Tech. Rep., June 2008.

[3] A. J. Davidson, S. Chellappa, Raja, D. M. Dattelbaum, and C.-S. Yoo, "Pressure induced isostructural metastable phase transition of ammonium nitrate," *J. Phys. Chem. A*, vol. 115, no. 42, pp. 11 889–11 896, 2011.

[4] J. Dai, B. Clough, I.-C. Ho, X. Lu, J. Liu, and X.-C. Zhang, "Recent progresses in terahertz wave air photonics," *IEEE Trans. Terahertz Science and Tech.*, vol. 1, no. 1, pp. 274–281, 2011.

[5] L. Pacheco-Londoño, W. Ortiz-Rivera, O. Primera-Pedrozo, and S. Hernández-Rivera, "Vibrational spectroscopy standoff detection of explosives," *Analytical and Bioanalytical Chemistry*, vol. 395, pp. 323–335, 2009.

[6] M. Nambayah and T. I. Quickenden, "A quantitative assessment of chemical techniques for detecting traces of explosives at counter-terrorist portals," *Talanta*, vol. 63, no. 2, pp. 461 – 467, 2004.

[7] C. Wilson, "Improvised explosive devices (IEDs) in Iraq: Effects and countermeasures," Library of Congress, Washington D.C., Congressional Research Service Report RS22330, Feb 2006.

[8] C. Griffith, "Unmanned aerial vehicle-mounted high sensitivity rf receiver to detect improvised explosive devices," Master's thesis, Naval Postgraduate School, 2007.

[9] H. Sekiguchi and S. Seto, "Proposal of an information signal measurement method in display image contained in electromagnetic noise emanated from a personal computer," in *Proc. IEEE Instrum. and Measure. Tech. Conf.*, 2008, pp. 1859–1863.

[10] "Title 47–Telecommunication §15," Code of Federal Regulations, FCC, Oct 1998.

[11] I. Smith and M. Coderre, "The continuing war against ieds," *WSTIAC Quarterly*, vol. 8, no. 2, pp. 3–6, April 2008.

[12] C. Stagner, A. Conrad, C. Osterwise, D. Beetner, and S. Grant, "A practical superheterodyne-receiver detector using stimulated emissions," *IEEE Trans. Instrum. Meas.*, vol. 60, no. 4, pp. 1461–1468, 2011. [Online]. Available: http://dx.doi.org/10.1109/TIM.2010.2101330.

[13] C. Stagner, M. Halligan, C. Osterwise, D. Beetner, and S. Grant, "Locating noncooperative radio receivers using wideband stimulated emissions," *IEEE Trans. Instrum. Measure.*, vol. 62, no. 3, pp. 667–674, 2013. [Online]. Available: http://dx.doi.org/10.1109/TIM.2012.2219141.

[14] D. Beetner, S. Seguin, and H. Hubing, "Electromagnetic emissions stimulation and detection system," U.S. Patent 7 464 005, 2008.

[15] B. Wild and K. Ramchandran, "Detecting primary receivers for cognitive radio applications," in *Proc. 1st IEEE Int'l Symp. DySPAN*, Nov. 2005, pp. 124–130.

[16] A. Shaik, H. Weng, X. Dong, T. Hubing, and D. Beetner, "Matched filter detection and identification of electronic circuits based on their unintentional radiated emissions," in *Proc. IEEE ISEMC*, vol. 3, 2006.

[17] S. Seguin, "Detection of low cost radio frequency receivers based on their unintended electromagnetic emissions and an active stimulation," Ph.D. dissertation, Missouri S&T, 2009. [Online]. Available: http://scholarsmine.mst.edu/thesis/pdf/Seguin_09007dcc80708216.pdf.

[18] R. Bracewell, *The Fourier Transform and Its Applications*, 3rd ed. McGraw-Hill, 1999, p. 108.

[19] T. Nguyen, S. Koppen, J. Ely, R. Williams, L. Smith, M. Salud, L. Martin, and V. Hampton, "Portable wireless LAN device and two-way radio threat assessment for aircraft VHF communication radio band," *NASA Langley Res. Center, NASA/TM-2004-213010*, 2004.

[20] R. Oki and T. Ebisawa, "Double Superheterodyne Receiver," U.S. Patent 4 395 777, 1983.

[21] P. Ferrari, A. Flammini, and E. Sisinni, "Introducing the Wireless Ultra Smart Sensor," in *Proc. IEEE I2MTC*, 2009, pp. 1304–1308.

[22] "Title 47–Telecommunication §95a," Code of Federal Regulations, FCC, Oct 1998.

[23] H. So, Y. Chan, Q. Ma, and P. Ching, "Comparison of various periodograms for sinusoid detection and frequency estimation," *IEEE Trans. AES*, vol. 35, no. 3, pp. 945–952, 2002.

[24] G. Turin, "An introduction to matched filters," *IRE Trans. Inf. Theory*, vol. 6, no. 3, pp. 311–329, June 1960.

[25] N. Levanon and E. Mozeson, *Radar Signals*. Wiley, 2004, ch. 4, p. 57.

[26] K. Chan and S. Judah, "A beam scanning frequency modulated continuous wave radar," *IEEE Trans. Instrum. Meas.*, vol. 47, no. 5, pp. 1223–1227, 2002.

[27] K. Barbé and W. V. Moer, "Automatic detection, estimation, and validation of harmonic components in measured power spectra: All-in-one approach," *IEEE Trans. Instrum. Meas.*, 2011, to be published.

[28] N. Patwari, A. Hero III, M. Perkins, N. Correal, and R. O'dea, "Relative location estimation in wireless sensor networks," *IEEE Trans. Sig. Proc.*, vol. 51, no. 8, pp. 2137–2148, 2003.

[29] F. Moseley, "The automatic radio direction finder," *IRE Trans. Aeronautical and Navigational Electronics*, no. 4, pp. 4–11, 1955.

[30] A. Kalis and T. Antonakopoulos, "Direction finding in IEEE802.11 wireless networks," *IEEE Trans. Instrum. Meas.*, vol. 51, no. 5, pp. 940–948, 2002.

[31] A. Paulraj, R. Roy, and T. Kailath, "Estimation of signal parameters via rotational invariance techniques–esprit," in *Proc. IEEE Asilomar Conf. Circuits, Systems and Computers*, 1985, pp. 83–89.

[32] R. Muhamed and T. Rappaport, "Comparison of conventional subspace based doa estimation algorithms with those employing property-restoral techniques: simulation and measurements," in *Proc. IEEE Int'l. Conf. Universal Personal Communications*, vol. 2, 1996, pp. 1004–1008.

[33] S. Gleason and D. Gebre-Egziabher, *GNSS Applications and Methods*. Artech, 2009, ch. 3, pp. 56–62.

[34] R. Ziemer and W. Tranter, *Principles of communications systems, modulation, and noise*, 6th ed. Wiley, 2010, ch. 3, pp. 133–136.

[35] M. Skolnik, "Theoretical accuracy of radar measurements," *IRE Trans. Aeronautical and Navigational Electronics*, no. 4, pp. 123–129, 1960.

[36] D. Noble, "The history of land-mobile radio communications," *Proc. IRE*, vol. 50, no. 5, pp. 1405–1414, May 1962.

[37] W. Swinyard, "The development of the art of radio receiving from the early 1920's to the present," *Proc. IRE*, vol. 50, no. 5, pp. 793–798, 1962.

[38] J. Schoukens, R. Pintelon, and Y. Rolain, "Broadband versus stepped sine FRF measurements," *IEEE Trans. Instrum. Meas.*, vol. 49, no. 2, pp. 275–278, 2000.

[39] M. Skolnik, *Radar handbook*, 2nd ed. N.Y.: McGraw-Hill, 1990.

[40] A. Stove, "Linear FMCW radar techniques," in *Proc. Inst. Elect. Eng.—Radar and Signal Process. F*, vol. 139, no. 5, 1992, pp. 343–350.

[41] N. Levanon and E. Mozeson, *Radar Signals.* Wiley, 2004, ch. 10, pp. 318–323.

[42] I. Komarov and S. Smolskiy, *Fundamentals of short-range FM radar.* Norwood, MA: Artech, 2003, ch. 2, pp. 11–26.

[43] A. Wojtkiewicz, J. Misiurewicz, M. Nałecz, K. Jedrzejewski, and K. Kulpa, "Two-dimensional signal processing in fmcw radars," in *Proc. XX KKTOiUE*, 1997, pp. 475–480.

[44] M. Skolnik, *Introduction to Radar*, 2nd ed. McGraw-Hill, 1981, no. 1, ch. 4, pp. 101–106.

[45] S. Piper, "Receiver frequency resolution for range resolution in homodyne fmcw radar," in *Proc. IEEE Telesystems Conf.*, 1995, pp. 169–173.

[46] V. Winkler, "Range doppler detection for automotive fmcw radars," in *Proc. IEEE EuRAD*, 2007, pp. 1445–1448.

[47] S. Kay, *Modern spectral estimation: theory and application.* Prentice Hall, 1988.

[48] M. Bouchard, D. Gingras, Y. De Villers, and D. Potvin, "High resolution spectrum estimation of fmcw radar signals," in *Proc. IEEE Workshop Stat. Sig. and Array Process.*, 1994, pp. 421–424.

[49] P. Pace, *Detecting and classifying low probability of intercept radar.* Artech, 2004, vol. 1, no. 2, ch. 4, pp. 83–85.

[50] T. Rappaport, J. Reed, and B. Woerner, "Position location using wireless communications on highways of the future," *IEEE Comm. Mag.*, vol. 34, no. 10, pp. 33–41, 1996.

[51] L. Cong and W. Zhuang, "Non-line-of-sight error mitigation in tdoa mobile location," in *Proc. IEEE Global Telecom. Conf.*, vol. 1, 2001, pp. 680–684.

[52] M. Wellens, J. Wu, and P. Mahonen, "Evaluation of spectrum occupancy in indoor and outdoor scenario in the context of cognitive radio," in *Proc. IEEE Int'l Conf. Cognitive Radio Oriented Wireless Networks and Comm.*, 2007, pp. 420–427.

[53] A. Saleh and R. Valenzuela, "A statistical model for indoor multipath propagation," *IEEE J. Selected Areas in Communications*, vol. 5, no. 2, pp. 128–137, 1987.

[54] J. Bard and F. Ham, "Time difference of arrival dilution of precision and applications," *IEEE. Trans. Sig. Proc.*, vol. 47, no. 2, pp. 521–523, 1999.

[55] S. Li, H. Bishnoi, J. Whiles, P. Ng, H. Weng, D. Pommerenke, and D. Beetner, "Development and validation of a microcontroller model for EMC," in *Proc. Int'l Symp. Electromagn. Compat–Europe*, 2008, pp. 1–6.

[56] S. Orfanidis, *Optimum signal processing: An introduction*, 2nd ed. N.Y.: McGraw-Hill, 1988, ch. 6, pp. 248–259.

[57] N. Ravirala, "Device signal detection methods and time frequency analysis," Master's thesis, University of Missouri–Rolla, 2007. [Online]. Available: http://scholarsmine.mst.edu/thesis/pdf/Ravirala_09007dcc803fea67.pdf.

[58] R. Zelinski, "A microphone array with adaptive post-filtering for noise reduction in reverberant rooms," in *IEEE Int'l. Conf. Acoustics, Speech, and Sig. Proc.*, vol. 5, apr 1988, pp. 2578 – 2581.

[59] I. Flintoft, A. Marvin, M. Robinson, K. Fischer, and A. Rowell, "The re-emission spectrum of digital hardware subjected to emi," *IEEE Trans. Electromagnetic Compatibility*, vol. 45, no. 4, pp. 576–585, 2003.

[60] K. Hu, H. Weng, D. Beetner, D. Pommerenke, J. Drewniak, K. Lavery, and J. Whiles, "Application of chip-level emc in automotive product design," in *Electromagnetic Compatibility, 2006. EMC 2006. 2006 IEEE International Symposium on*, vol. 3, 2006, pp. 842–848.

[61] D. Panyasak, G. Sicard, and M. Renaudin, "A current shaping methodology for lowering EM disturbances in asynchronous circuits," *Microelectronics journal*, vol. 35, no. 6, pp. 531–540, 2004.

[62] Y. Fu, G. Burbui, and T. Hubing, "An improved model for representing current waveforms in cmos circuits," in *Proc. IEEE Int'l. Symp. Electromagnetic Compatibility*, 2007, pp. 289–292.

[63] M. Schroeder and B. Atal, "Code-excited linear prediction (celp): High-quality speech at very low bit rates," in *IEEE Int'l Conf. Acoustics, Speech, and Sig. Proc.*, vol. 10, 1985, pp. 937–940.

[64] D. Percival and A. Walden, *Spectral analysis for physical applications.* Cambridge University Press, 1993, ch. 9, pp. 391–455.

[65] M. H. Hansen and B. Yu, "Model selection and the principle of minimum description length," *Journal of the American Statistical Association*, vol. 96, no. 454, pp. 746–774, 2001.

[66] A. N. Iyer, M. Gleiter, B. Y. Smolenski, and R. E. Yantorno, "Structural usable speech measure using lpc residual," in *International Symposium on Intelligent Signal Processing and Communication Systems*, vol. 2, no. 3, 2003, pp. 236–240.

[67] D. Percival and A. Walden, *Spectral analysis for physical applications.* Cambridge University Press, 1993, ch. 3, pp. 56–125.

[68] P. Welch, "The use of fast fourier transform for the estimation of power spectra: a method based on time averaging over short, modified periodograms," *IEEE Trans. Audio and Electroacoustics*, vol. 15, no. 2, pp. 70–73, 1967.

[69] D. Percival and A. Walden, *Spectral analysis for physical applications.* Cambridge University Press, 1993, ch. 7, pp. 331–377.

[70] A. De Cheveigné and H. Kawahara, "Yin, a fundamental frequency estimator for speech and music," *J. of Acoustical Society of America*, vol. 111, p. 1917, 2002.

[71] T. Shimamura and H. Kobayashi, "Weighted autocorrelation for pitch extraction of noisy speech," *IEEE Trans. Speech and Audio Processing*, vol. 9, no. 7, pp. 727–730, 2001.

[72] M. Hinich, "Detecting a hidden periodic signal when its period is unknown," *IEEE Trans. Acoustics, Speech and Sig. Proc.*, vol. 30, no. 5, pp. 747–750, 1982.

[73] M. Noll, "Pitch determination of human speech by the harmonic product spectrum, the harmonic sum spectrum, and a maximum likelihood estimate," in *Proc. Symposium on Computer Processing Communications*, 1969, pp. 779–797.

[74] D. Staelin, "Fast folding algorithm for detection of periodic pulse trains," *Proc. IEEE*, vol. 57, no. 4, pp. 724–725, 1969.

[75] V. Kondratiev, M. McLaughlin, D. Lorimer, M. Burgay, A. Possenti, R. Turolla, S. Popov, and S. Zane, "New limits on radio emission from x-ray dim isolated neutron stars," *The Astrophysical Journal*, vol. 702, no. 1, p. 692, 2009.

[76] S. Davies, "An improved test for periodicity," *Monthly Notices of the Royal Astronomical Society*, vol. 244, pp. 93–95, 1990.

[77] S. Larsson, "Parameter estimation in epoch folding analysis," *Astronomy and Astrophysics Supplement Series*, vol. 117, no. 1, pp. 197–201, 1996.

[78] C. S. Patel, G. L. Stuber, and T. G. Pratt, "Comparative analysis of statistical models for the simulation of rayleigh faded cellular channels," *IEEE Trans. Commun.*, vol. 53, no. 6, pp. 1017–1026, 2005.

[79] J. G. Proakis and D. G. Manolakis, *Digital communications*, 5th ed. McGraw-hill, 2008, ch. 13, pp. 869–884.

[80] M. H. Zweig and G. Campbell, "Receiver-operating characteristic (roc) plots: a fundamental evaluation tool in clinical medicine." *Clinical chemistry*, vol. 39, no. 4, pp. 561–577, 1993.

[81] H. L. Van Trees, *Detection, estimation, and modulation theory.* Wiley, 2001, ch. 2, pp. 23–46.

[82] M. Xiangwei, G. Jian, and W. Xinzheng, "Order statistics for negative exponential distribution and its applications," in *Proc. IEEE Int'l. Conf. Neural Net. and Sig. Proc.*, vol. 1, 2003, pp. 720–722.

[83] J. Saniie and D. T. Nagle, "Analysis of order-statistic cfar threshold estimators for improved ultrasonic flaw detection," *IEEE Trans. Ultrasonics, Ferroelectrics and Frequency Control*, vol. 39, no. 5, pp. 618–630, 1992.

[84] J. G. Proakis and D. G. Manolakis, *Digital communications*, 5th ed. McGraw-hill, 2008, ch. 10, pp. 689–731.

[85] H. Rohling, "Radar cfar thresholding in clutter and multiple target situations," *IEEE Trans. Aero. and Elec. Sys.*, no. 4, pp. 608–621, 1983.

[86] F. Walls and J. Gagnepain, "Environmental sensitivities of quartz oscillators," *IEEE Trans. Ultrasonics, Ferroelectrics and Frequency Control*, vol. 39, no. 2, pp. 241–249, 1992.

[87] C. D. Hoekstra, "Frequency modulation of system clocks for emi reduction," Hewlett Packard, Tech. Rep., 1997.

[88] K. B. Hardin, J. T. Fessler, and D. R. Bush, "Spread spectrum clock generation for the reduction of radiated emissions," in *Proc. IEEE Int'l. Symp. Electromagnetic Compatibility*, 1994, pp. 227–231.

[89] W. Gardner, "Exploitation of spectral redundancy in cyclostationary signals," *IEEE Sig. Proc. Mag.*, vol. 8, no. 2, pp. 14 –36, april 1991.

[90] P. Pace, *Detecting and classifying low probability of intercept radar.* Artech, 2004, vol. 1, ch. 15, pp. 513–550.

[91] F. Tuffner, J. Pierre, and R. Kubichek, "Computationally efficient updating of a weighted welch periodogram for nonstationary signals," in *Proc.* 51^{st} *MWSCAS*, Aug 2008, pp. 799–802.

[92] S. Seguin, "Detection of regenerative receivers based on the modulation of their unintended emissions," in *Detection of low cost radio frequency receivers based on their unintended electromagnetic emissions and an active stimulation*, 2009, ph.d dissertation 3, pp. 37–52. [Online]. Available: http://scholarsmine.mst.edu/thesis/pdf/Seguin_09007dcc80708216.pdf.

[93] A. V. Oppenheim, R. W. Schafer, and J. R. Buck, *Discrete-time signal processing*, 2nd ed. Pearson, 1999, ch. 4, pp. 211–223.

[94] T. Ulversoy, "Software defined radio: Challenges and opportunities," *IEEE Comm. Surveys & Tutorials*, vol. 12, no. 4, pp. 531–550, 2010.

[95] N. Levanon and E. Mozeson, *Radar Signals.* Wiley, 2004, ch. 1, pp. 1–19.

VITA

Colin Blake Stagner, better known to his friends and colleagues as "Chibi," was born in mid-1986 in a small college town. At a young age, Colin taught himself programming, graph theory, and networking protocols by writing automatic game-playing scripts for bulletin board system games. Before graduating from high school, he had written his first database-driven website, which saw active use for many years thereafter.

As an undergraduate, Colin contributed to university research both directly, through the Computer Science department, and indirectly as a circulation staff member at the Curtis Laws Wilson library. He also served as an officer of the Society of Women Engineers for three consecutive years. Colin was awarded a Bachelor of Science degree in 2008 by the University of Missouri–Rolla, which is now known as the Missouri University of Science and Technology (S&T). He graduated summa cum laude with a degree in Computer Science.

Soon after graduation, Colin returned to his alma mater to begin work on his doctorate degree. He changed majors after accepting a Graduate Research Assistant position from Dr. Steve Grant in the Electrical Engineering department. There, he studied digital signal processing—a discipline which melds computer and electric systems with the physical world. His principal contribution to the field was a software-defined radar system for locating radio receivers. As part of a class project, he also developed a digital communications receiver for amateur radio, which he uses to receive transmissions from the International Space Station. He became Dr. Colin Stagner in December 2013 when he was awarded a Ph.D. from S&T.